# A Compartmentalized Model of Multiphase Chemical Kinetics

Alexander M. Prophet,[1] and Kevin R. Wilson[1*]

[1]*Chemical Sciences Division, Lawrence Berkeley National Laboratory, Berkeley, CA 94720*

Abstract

There are significant challenges in predicting multiphase chemical kinetics due to the complex coupling of reaction and mass transport across a phase boundary (*i.e.* interface). Here we describe a framework for predicting multiphase kinetics that embeds the elementary kinetic steps of reaction, solvation and diffusion into a coarse grain spatial description of two phases. The model is constructed to bridge the short-timescale interfacial dynamics observed in molecular simulations with the longer timescales observed in kinetic experiments. A simple set of governing differential equations is presented, which when solved numerically or analytically, yield accurate predictions of multiphase kinetics in microdroplets. Although the equations are formulated for gas-liquid reactions, the underlying conceptual framework is general and can be applied to transformations in other two-phase systems (solid-liquid, liquid-liquid, etc.).
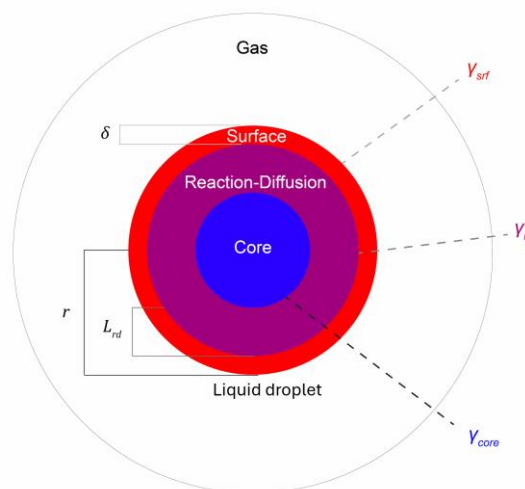
*Correspondence to krwilson@lbl.gov

1

I. Introduction

Chemistry invariably invokes images of beakers and flasks filled with liquids, with the chemist mixing, stirring, and heating reactants in various proportions. Wet chemistry of this type, involving a chemical reaction in a single phase, is vanishingly rare in natural systems—from the environment that surrounds us to the mechanics of our own biology. On a global scale, multiphase processes on the Earth's surface and in its atmosphere span an incredibly broad range, from familiar phenomena like the hydrologic cycle and weather patterns to more subtle effects like the influence of ground emissions on cloud formation and the oxidizing capacity of the atmosphere.[1, 2] Multiphase processes are central for biology, as virtually all organisms rely on gas-liquid or solid-liquid exchange with the environment to maintain homeostasis. The boundary of the cell wall permits the electrochemical gradient necessary for cellular function and recent work has highlighted an emerging understanding of liquid-liquid phase separation within the cell.[3-5] Furthermore, solute transport across polymer membranes to achieve selective separations is of immense technological importance for future clean energy applications.[6] In all of these systems understanding how multiphase transformations emerge from the complex coupling of chemical reactions with mass transport across phase boundaries remains a substantial challenge.

Here we present a general approach for quantifying and predicting multiphase kinetics using a discretized or "compartmentalized" representation of chemistry spanning two phases. These methods grew out of explicit kinetic simulations of multiphase chemistry in aerosols, emulsions[7] and droplets[8-12] implemented in a stochastic reaction diffusion simulator, Kinetiscope©.[13] This work builds upon our previous efforts[11, 12] to develop a simple, physically realistic framework for predicting multiphase aerosol chemistry. Here we expand upon this framework to include more sophisticated descriptions of gas and liquid phase diffusion. The result is a "compartmentalized" description of kinetics expressed as a simple set of coupled differential equations, which when solved numerically (or using approximate closed form solutions) accurately predict surface and bulk uptake coefficients as well as multiphase reaction kinetics in aerosols and droplets. Although the current work is formulated for gas-liquid reactive uptake, the conceptual features of the framework can be readily adapted to kinetics in liquid-liquid, liquid-solid, or gas-solid systems.

II. A Compartmentalized Description of Multiphase Chemical Kinetics

2

As illustrated in Fig. 1A, any multiphase kinetic model starts with the same basic framework. At equilibrium and in the absence of a reaction, X (in this case a gas phase molecule) is partitioned between the gas (g) and liquid (*bulk*) phases. The concentrations of X in the gas ($[X_{(g,\infty)}]$) and liquid ($[X_{(blk)}]$) are governed by differences in solvation free energies and described by a Henry's Law constant, ($H_{cc}^{gb} = [X_{(blk)}]/[X_{(g,\infty)}]$) where cc denotes the dimensionless form. Prior to the widespread use of molecular dynamics (MD) simulations, the concentration of X at the
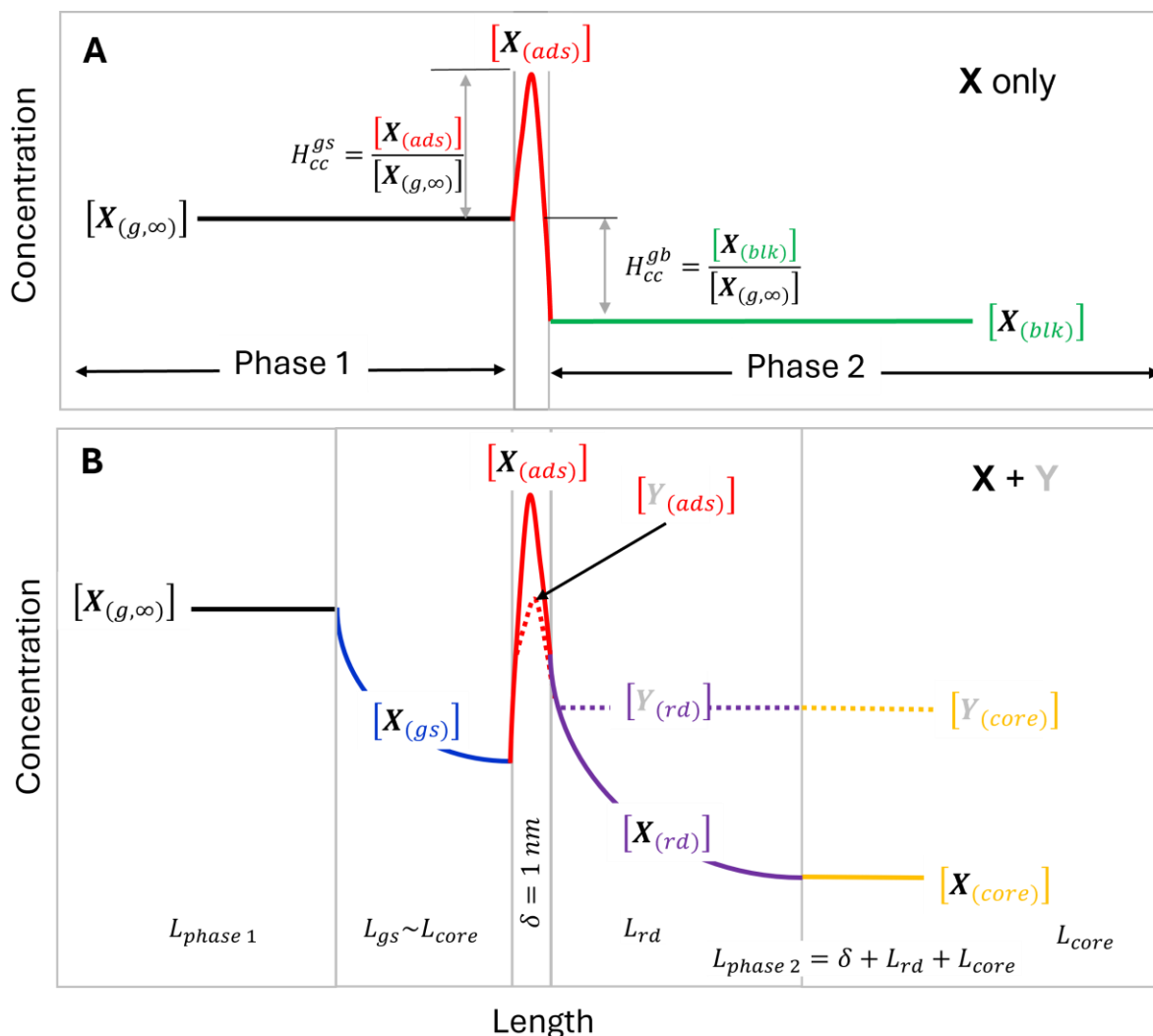
Figure 1: Concentration profiles of gas phase solute X and liquid phase solute Y in a two-phase system. (A) For the case where there is no reaction the equilibrium concentrations of X in phase 1 (black), phase 2 (green) and at the biphasic interface (red) are governed by Henry's law constants (H_{cc}). (B) Steady state concentration profiles and gradients in X that form in the gas (blue) and liquid phases (purple) due to its reaction with Y. Also shown are compartments of length (L), which are distinguished by changes or gradients in X.

3

droplet interface (*i.e.,* X$_{(ads)}$) was assumed to be that of either the gas or liquid phase. However, simulations show that this is often not the case, with trace gases exhibiting negative surface solvation free energies relative to the gas and liquid phases and thus, as illustrated in Fig. 1A, increased density the interface (*i.e.,* H_{cc}^{gs} = [X$_{(ads)}$]/[X$_{(g,\infty)}$] > 1). At equilibrium a two-phase system, consisting of a single mutually soluble species X, can be envisioned as three distinct spatial regions or compartments each with a characteristic [X] (*i.e.,* [X$_{(g,\infty)}$], [X$_{(ads)}$] and [X$_{(blk)}$]).

In the presence of a liquid solute Y that reacts with X, the equilibrium concentration of X during the reaction is perturbed as illustrated in Fig. 1B. Depending upon the surface activity of Y and the overall reaction rate relative to the mass transport timescales, concentration gradients of X (and potentially Y) can form at the gas and liquid sides of the interface. This means that concentrations of X in the gas and liquid phase are no longer uniform as depicted in Fig. 1 A and additional compartments or regions are needed to represent these gradients. For example, fast surface reactions readily deplete the local gas phase concentration above the interface such that [X$_{(g,\infty)}$] > [X$_{(gs)}$]. Similarly, reactions that substantially attenuate the flux of X entering the liquid, produce gradients in X such that [X$_{(rd)}$] > [X$_{(core)}$].

Rather than dividing the two phase system up into a large number of small regions or layers, our approach is to coarse grain the system into a few key, kinetically relevant regions or compartments.[12] Unlike kinetic multilayer models,[14-19] we consider only the average concentrations of X and Y within each region, rather than attempting to capture the explicit functional form of the concentration gradients. These "kinetically relevant" regions represent places where the concentrations of X or Y are distinct or where there is the potential for gradients in X and Y to form due to the strong coupling of reaction and diffusion. These compartments (Fig. 1B), each with a characteristic spatial dimension, correspond to the gas phase, gas-surface region, the interface, the reacto-diffusive volume below the interface and the inner core of the droplet.

The interface length or thickness (δ) is assumed to be ~ 1 nm, which approximates the width of the density profile in MD simulations of the air-water interface.[20-22] The length of the reacto-diffusive compartment (L_{rd}) depends upon the X + Y reaction rate,

$$L_{rd} = \sqrt{\frac{D_{(aq)}^{X}}{k_{rxn}^{bulk} \cdot [Y_{blk}]}}. \qquad \text{Eq. (1)}$$

4

$D_{(aq)}^X$, k_{rxn}^{blk}, and [Y$_{(blk)}$] are the liquid phase diffusion constant of X, the rate coefficient for the X + Y reaction and the bulk concentration of solute Y, respectively. The length of the core region for a spherical aerosol with radius, r, is $L_{core} = r - \delta - L_{rd}$. Both L_{rd} and L_{core} are dynamic quantities that evolve during a reaction as Y is consumed. For reactions that are slow relative to diffusion, $L_{rd} \sim$ r and hence the length of the core tends to zero as $L_{rd} \rightarrow r$. To account for this limit a "transition function" (L'_{rd}) is needed,

$$L'_{rd} = \frac{L_{rd}}{1 + r^{-1} \cdot L_{rd}} \qquad \text{Eq. (2)}$$

which closely approximates the reaction-diffusion length when $L_{rd} < r$ and asymptotes to r when $L_{rd} > r$, as shown in Fig. S1.

The model described consists of three compartments: the surface (*srf*), reacto-diffusive (*rd*) and inner core (*core*) volumes, with respective subscript denotations indicated in parentheses. As noted above, a near-surface compartment can also be implemented if the gas dynamics near the surface are of interest. For simplicity we neglect this region and assume gas-phase diffusion occurs directly to and from the droplet interface as explored in depth in Sect. V.A, with further details included in Appendix A. These sections illustrate how the gas-phase itself is defined directly as acting upon the surface compartment, such that no explicit "gas" compartment is necessary to execute the model.

As shown in Fig. 2, our model of multiphase chemistry is formulated as a sequence of elementary kinetic steps embedded in three compartments. These steps describe the uptake of X and its reaction with Y. In addition to these chemical equilibria and reaction steps, diffusion pathways are included that describe the transfer of X and Y between compartments. This description aims to connect continuum descriptions of diffusive transport[23, 24] with the molecularity of individual kinetic steps[25-28] that govern trace gas uptake and reaction.

5

As illustrated in Fig. 2, trace gas uptake and reaction occurs when a gas phase molecule $X_{(g,\infty)}$ diffuses to the near surface region (indicated with subscript *gs*) of the droplet or interface with a rate constant of k_{Xdiff}^{gas}, producing the species labeled $X_{(gs)}$. This step is modeled directly in the surface compartment since, as noted above, we assume that diffusion between the interface and the near surface is instantaneous. The backward rate constant for gas phase diffusion away from the near surface (*i.e.,* $X_{(gs)} \to X_{(g,\infty)}$) is also k_{Xdiff}^{gas}. Once near the surface, $X_{(gs)}$ can adsorb to the
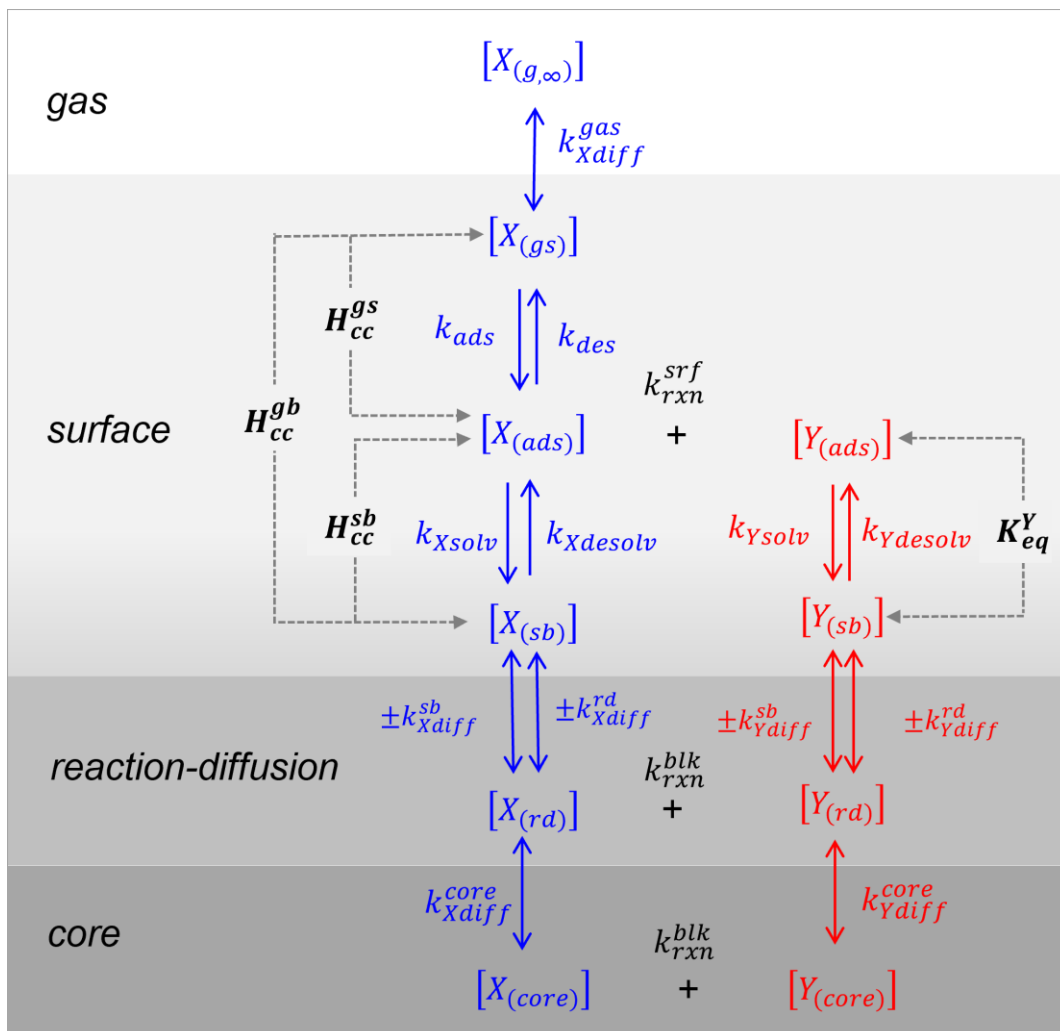
Figure 2: Conceptual diagram of the coarse grain kinetic framework. On the left, the multiphase system is divided up into kinetically relevant regions: gas (*g*), surface (*s*), reacto-diffusive (*rd*) volume and core (*core*). Embedded within these compartments are elementary kinetic steps that describe X adsorption (*ads*), desorption (*des*), solvation (*solv*) and desolvation (*desolv*). In addition, there are steps that describe gas phase diffusion of X (k_{xdiff}^{gas}) and liquid phase diffusion of X and Y (e.g., k_{xdiff}^{liquid}). H_{cc} are the coupled equilibria that describe the partitioning of X between the gas, surface and bulk liquid. K_{eq} described the surface partition of Y between the bulk and interface.

6

interface ($X_{(gs)} \rightarrow X_{(ads)}$, k_{ads}) becoming thermally accommodated (*i.e.,* $X_{(ads)}$). There is some probability that $X_{(ads)}$ can then desorb from the interface ($X_{(ads)} \rightarrow X_{(gs)}$, k_{des}) back into the gas phase. This pair of adsorption/desorption steps comprise the gas-surface equilibrium constant, H_{cc}^{gs}, formulated as a Henry's law coefficient specifically connecting the gas to the surface. Instead of desorption, $X_{(ads)}$ can instead undergo solvation ($X_{(ads)} \rightarrow X_{(sb)}$, k_{Xsolv}). Once solvated, $X_{(sb)}$ may desolvate back to form $X_{(ads)}$ ($X_{(sb)} \rightarrow X_{(ads)}$, $k_{Xdesolv}$), defining a pair of reversible steps with corresponding rate coefficients k_{Xsolv} and $k_{Xdesolv}$. These coefficients make up a second Henry's law equilibrium constant (*i.e.,* H_{cc}^{sb}), connecting surface and bulk concentrations of X. Rather than undergo desolvation, $X_{(sb)}$ can diffuse into the subsurface reacto-diffusive volume ($X_{(rd)}$) at a rate proportional to a diffusional rate constant, k_{Xdiff}^{rd}. Similarly, $X_{(rd)}$ can diffuse out of the reacto-diffusive volume back to the surface, or into the inner core of the aerosol becoming $X_{(core)}$. As will be shown below, partitioning of X between the gas, interface and bulk liquid is described using the Langmuir equation and the Henry's law constants illustrated in Fig. 2.

For a non-volatile solute (Y) the reaction with X occurs at the interface, via a Langmuir Hinshelwood mechanism ($X_{(ads)} + Y_{(ads)}$), in the reacto-diffusive volume ($X_{(rd)} + Y_{(rd)}$), and in the core of the droplet ($X_{(core)} + Y_{(core)}$). As discussed in Sect. V.E, the rate constant for the interfacial reaction (k_{rxn}^{srf}) need not be the same as that for a bulk reaction (k_{rxn}^{blk}) occurring in the reacto-diffusive and core regions of the droplet. Partitioning of Y between the bulk ($Y_{(rd)}$) and interface ($Y_{(ads)}$) is treated identically to that of X and is described by the kinetic steps of solvation/desolvation in the Langmuir equation (see Sect. V.C). Here we assume diffusion of Y in the solvent is rapid and remains uniformly distributed throughout the bulk regions (*rd* and *core*) of the droplet; $[Y_{(rd)}] = [Y_{(core)}] = [Y_{(blk)}]$. This is assumption is generally valid for reactions with "trace gases" where $[Y] \gg [X]$. A similar model framework can be used to treat simultaneous diffusion and reaction of both X and Y, as will be explored in future work.

In summary, in addition to the reaction (X+Y) and reversible diffusion steps there is an equilibrium governing the partitioning of X between the gas and interface (H_{cc}^{gs}) and two additional equilibria that govern the partitioning X (H_{cc}^{sb}) and Y (K_{eq}^{Y}) between the bulk and interface (Fig. 2). These equilibria are coupled and respond dynamically to the presence of the X+Y reaction in each compartment. These steps and the associated differential equations embedded in the

7

compartmentalized representation of the two-phase system are the basis for the kinetic model described below.

III. Governing Equations

In most aerosol and droplet experiments, multiphase kinetics are quantified by either the loss of gas phase X or condensed phase Y. The majority of experiments don't distinguish between surface and bulk concentrations, but rather only measure total concentrations of X and/or Y ($[X_{(total)}]$ and $[Y_{(total)}]$) versus time, which can be expressed as a bimolecular rate law,

$$\frac{d[Y_{(total)}]}{dt} = \frac{d[X_{(total)}]}{dt} = -k_{rxn} \cdot [Y_{(total)}][X_{(total)}] = \frac{3 \cdot \bar{c} \cdot [X_{(g,\infty)}] \cdot \gamma_{total}}{4 \cdot r} \qquad \text{Eq. (3)}$$

For a gas-liquid reaction, the rate law in Eq. (3) is proportional to the total uptake coefficient (γ_{total}), the gas phase collision frequency computed for a droplet with radius (r), and the mean speed ($\bar{c}$) of X in the gas phase. The total rate law and uptake coefficient in Eq. (3) can be expressed as a sum of the contributions from the three spatial regions (*srf*, *rd*, and *core*) described above, each of which contributes $[Y_{(total)}]_t$ and γ_{total},

$$\frac{d[Y_{(total)}]^{srf}}{dt} = -k_{rxn}^{srf} \cdot [Y_{(ads)}][X_{(ads)}]\left(\frac{V_{srf}}{V_{total}}\right) = \frac{3 \cdot \bar{c} \cdot [X_{(g,\infty)}] \cdot \gamma_{srf}}{4 \cdot r} \qquad \text{Eq. (4)}$$

$$\frac{d[Y_{(total)}]^{rd}}{dt} = -k_{rxn}^{blk} \cdot [Y_{(total)}][X_{(rd)}]\left(\frac{V_{rd}}{V_{total}}\right) = \frac{3 \cdot \bar{c} \cdot [X_{(g,\infty)}] \cdot \gamma_{rd}}{4 \cdot r} \qquad \text{Eq. (5)}$$

$$\frac{d[Y_{(total)}]^{core}}{dt} = -k_{rxn}^{blk} \cdot [Y_{(total)}][X_{(core)}]\left(\frac{V_{core}}{V_{total}}\right) = \frac{3 \cdot \bar{c} \cdot [X_{(g,\infty)}] \cdot \gamma_{core}}{4 \cdot r} \qquad \text{Eq. (6)}$$

Solving Eqs. (4)-(6) for the uptake coefficient in each compartment yields,

$$\gamma_{srf} = \frac{4 \cdot r \cdot k_{rxn}^{srf} \cdot [X_{(ads)}][Y_{(ads)}]}{3 \cdot \bar{c} \cdot [X_{(g,\infty)}]}\left(\frac{V_{srf}}{V_{total}}\right), \qquad \text{Eq. (7)}$$

$$\gamma_{rd} = \frac{4 \cdot r \cdot k_{rxn}^{blk} \cdot [X_{(rd)}][Y_{(total)}]}{3 \cdot \bar{c} \cdot [X_{(g,\infty)}]}\left(\frac{V_{rd}}{V_{total}}\right), \qquad \text{Eq. (8)}$$

$$\gamma_{core} = \frac{4 \cdot r \cdot k_{rxn}^{blk} \cdot [X_{(core)}][Y_{(total)}]}{3 \cdot \bar{c} \cdot [X_{(g,\infty)}]}\left(\frac{V_{core}}{V_{total}}\right). \qquad \text{Eq. (9)}$$

whose sum is γ_{total},

$$\gamma_{total} = \gamma_{srf} + \gamma_{rd} + \gamma_{core} \qquad \text{Eq. (10)}$$

8

The contributions of Eqs. (4)-(9) to $[Y_{(total)}]_t$ and γ_{total} depend upon reaction rate coefficients (k_{rxn}^{srf} and k_{rxn}^{blk}), compartment volumes (V_{core}, V_{rd} and V_{srf}) and reactant concentrations in each compartment (*i.e.*, $[X_{(ads)}]$, $[Y_{(ads)}]$, $[X_{(rd)}]$, $[X_{(core)}]$, $[Y_{(total)}]$). As shown previously,[12] the product of the concentration and volume terms in Eqs. (4)-(9) is used to compute the fractional contribution of each compartment to the $[Y_{(total)}]_t$ and γ_{total}. For a sphere these volumes are,

$$V_{srf} = \frac{4}{3}\pi r^3 - \frac{4}{3}\pi(r-\delta)^3, \qquad \text{Eq. (11)}$$

$$V_{rd} = \frac{4}{3}\pi(r-\delta)^3 - \frac{4}{3}\pi(r-\delta-L'_{rd})^3, \qquad \text{Eq. (12)}$$

$$V_{core} = \frac{4}{3}\pi(r-\delta-L'_{rd})^3, \qquad \text{Eq. (13)}$$

$$V_{total} = \frac{4}{3}\pi r^3. \qquad \text{Eq. (14)}$$

The six differential equations that describe the evolution of [X] and [Y] illustrated mechanistically in Fig. 2 are,

$$\frac{d[X_{(gs)}]}{dt} = k_{diff}^{gas}[X_{(g,\infty)}] + k_{des}[X_{(ads)}] - k_{diff}^{gas}[X_{(gs)}] - k_{ads}\frac{\Gamma_{\infty(X)}}{\delta}[X_{(gs)}] \qquad \text{Eq. (15)}$$

$$\frac{d[X_{(ads)}]}{dt} = k_{ads}\frac{\Gamma_{\infty(X)}}{\delta}[X_{(gs)}] + k_{Xdesolv}\frac{\Gamma_{\infty(X)}}{\delta}[X_{(sb)}] - k_{des}[X_{(ads)}] - k_{Xsolv}[X_{(ads)}] - k_{rxn}^{srf}[Y_{(ads)}][X_{(ads)}]$$

$$\text{Eq. (16)}$$

$$\frac{d[X_{(sb)}]}{dt} = k_{Xsolv}[X_{(ads)}] + k_{Xdiff}^{sb}[X_{(rd)}] - k_{Xdesolv}\frac{\Gamma_{\infty(X)}}{\delta}[X_{(sb)}] - k_{Xdiff}^{sb}[X_{(sb)}] \qquad \text{Eq. (17)}$$

$$\frac{d[X_{(rd)}]}{dt} = k_{Xdiff}^{rd}[X_{(sb)}] - k_{Xdiff}^{rd}[X_{(rd)}] - k_{rxn}^{blk}[Y_{(total)}][X_{(rd)}] \qquad \text{Eq. (18)}$$

$$\frac{d[X_{(core)}]}{dt} = k_{Xdiff}^{core}[X_{(rd)}] - k_{Xdiff}^{core}[X_{(core)}] - k_{rxn}^{blk}[Y_{(total)}][X_{(core)}] \qquad \text{Eq. (19)}$$

$$\frac{d[Y_{(total)}]}{dt} = -S\,k_{rxn}^{srf}[Y_{(ads)}][X_{(ads)}]\frac{V_{srf}}{V_{total}} - S\,k_{rxn}^{blk}[Y_{(total)}][X_{(rd)}]\frac{V_{rd}}{V_{total}} - S\,k_{rxn}^{blk}[Y_{(total)}][X_{(core)}]\frac{V_{core}}{V_{total}}$$

$$\text{Eq. (20)}$$

In Sect. V we discuss in detail how the rate coefficients that appear in these expressions are obtained for a given system. The $\left(\frac{\Gamma_{\infty(X)}}{\delta}\right)$ term in Eqs. (15)-(17) is the maximum concentration of

9

Langmuir adsorption sites at the interface, where $\frac{1}{\Gamma_{\infty(X)}}$ is proportional to the surface area of X (cm^2 molec.$^{-1}$) and δ is interface thickness (1 nm). A full discussion of how the Langmuir framework is used to describe the surface partitioning of X and Y is provided in Sects. V.B and V.C, respectively. Lastly, a stoichiometric factor (S) is included in Eq. (20) to provide a simple way to approximate the role of secondary chemistry when the loss of Y relative to X differs from 1:1. In Sect. VI, we numerically solve Eqs. (15)-(20) and validate the model results against prior experimental measurements of multiphase ozone reactions with a variety of aqueous solutes in microdroplets.

IV. Analytical Solutions

Approximate closed form solutions for both the uptake coefficients and reaction kinetics of [Y] can be obtained by applying steady-state approximations[12] to Eqs. (15)-(19). These derivations are shown in Sect. SI-2 of the Supplementary Information. The final closed form kinetic equations, shown below, are obtained using Lambert W functions[29] as previously reported.[12] Lambert W functions can be computed in *Mathematica* (Productlog Function), MATLAB (W function) and Python (lambertw function) using built in algorithms. Although we refer to our expressions as "closed-form" or "analytical," there appears to be no consensus as to whether Lambert W functions are strictly included in the general definition of closed-form solutions. Nevertheless, we adopt this convention in light of previous terminology.[30]

As shown previously,[12] deriving the time-dependent expressions for $[Y_{(total)}]_t$ relies on computing "steady-state" expressions for the trace gas X within each compartment. The general method can be summarized by first applying the steady-state approximation to Eqs. (15)-(19), to yield an expression for the concentration of X in each region $[X_{(region)}]$ as a function of $[Y_{(total)}]$. These steady-state expressions $[X_{(region)}]$ are then substituted into Eq. (20), which can then be integrated by separation of variables and solved for $[Y_{(total)}]_t$ as function of time t, radius r, gas concentration $[X_{(gas,\infty)}]$, and the rate coefficients outlined in Sect. II and detailed in Sect. VI. Only the final equations are shown below with a full derivation provided in Sect. SI-2 of the Supplementary Information.

The analytical expression for loss of Y due to reaction with X occurring only in the reacto-diffusive volume is,

$$[Y_{(total)}]_t^{rd} = \frac{\frac{\Gamma_{\infty(X)}}{\delta} \cdot k_{Xdesolv} \cdot k_{Xdiff}^{rd}}{\left(\frac{\Gamma_{\infty(X)}}{\delta} \cdot k_{Xdesolv} + k_{Xdiff}^{sb}\right) \cdot k_{rxn}^{blk}} \cdot W\left\{\frac{\left(\frac{\Gamma_{\infty(X)}}{\delta} \cdot k_{Xdesolv} + k_{Xdiff}^{sb}\right) \cdot k_{rxn}^{blk} \cdot [Y_{(total)}]_0}{\frac{\Gamma_{\infty(X)}}{\delta} \cdot k_{Xdesolv} \cdot k_{Xdiff}^{rd}} \cdot N_1\right\}$$

$$N_1 = exp\left(\frac{\left(\frac{\Gamma_{\infty(X)}}{\delta} \cdot k_{Xdesolv} + k_{Xdiff}^{sb}\right) \cdot k_{rxn}^{blk}[Y_{(total)}]_0}{k_{Xdiff}^{rd} \cdot \frac{\Gamma_{\infty(X)}}{\delta} \cdot k_{Xdesolv}} - \frac{k_{rxn}^{blk} \cdot k_{Xsolv} \cdot H_{cc}^{gs} \cdot S \cdot [X_{(g,\infty)}]}{\frac{\Gamma_{\infty(X)}}{\delta} \cdot k_{Xdesolv}} \cdot \frac{V_{rd}}{V_{total}} t\right). \qquad \text{Eq. (21)}$$

where $[Y_{(total)}]_0$ is the initial concentration of solute Y. As discussed in Sect. SI-2, Eq. (21) is obtained by considering reactivity in the *rd* region alone and neglecting the reactivity of the core region. This approximation is generally valid since, by definition, the majority of bulk reactivity occurs within the *rd* region. Reaction in the *core* accounts for up to ~10% of the total reactions for the special case where the $L_{rd} \approx L_{core}$.

The time-dependent expression for [Y*(total)*] due to only a surface reaction is,

$$[Y_{(total)}]_t^{srf} = \frac{\theta}{\frac{\Gamma_{\infty(Y)}}{\delta} \cdot K_{eq}^Y \cdot k_{rxn}^{srf} + K_{eq}^Y \cdot \theta} \cdot W\left\{\frac{\frac{\Gamma_{\infty(Y)}}{\delta} \cdot K_{eq}^Y \cdot k_{rxn}^{srf} + K_{eq}^Y \cdot \theta}{\theta}[Y_{(total)}]_0 \cdot N_2\right\}$$

$$N_2 = exp\left(\frac{\frac{\Gamma_{\infty(Y)}}{\delta} \cdot K_{eq}^Y \cdot k_{rxn}^{srf} + K_{eq}^Y \cdot \theta}{\theta}[Y_{(total)}]_0 - \frac{\left(\frac{k_{diff}^{gas} \cdot \frac{\Gamma_{\infty(X)}}{\delta} \cdot k_{ads}}{k_{diff}^{gas} + \frac{\Gamma_{\infty(X)}}{\delta} \cdot k_{ads}}\right) \cdot \frac{\Gamma_{\infty(Y)}}{\delta} \cdot K_{eq}^Y \cdot k_{rxn}^{srf} \cdot S \cdot [X_{(g,\infty)}]}{\theta} \cdot \frac{V_{srf}}{V_{total}} \cdot t\right)$$

$$\theta = k_{des} + k_{Xsolv} - \left(\frac{k_{des} \cdot \frac{\Gamma_{\infty(X)}}{\delta} \cdot k_{ads}}{k_{diff}^{gas} + \frac{\Gamma_{\infty(X)}}{\delta} \cdot k_{ads}}\right) - \left(\frac{k_{Xsolv} \cdot \frac{\Gamma_{\infty(X)}}{\delta} \cdot k_{Xdesolv}}{k_{Xdiff}^{sb} + \frac{\Gamma_{\infty(X)}}{\delta} \cdot k_{Xdesolv}}\right). \qquad \text{Eq. (22)}$$

The complete expression that includes reactions at both the surface and within the *rd* region is obtained by replacing $[Y_{(total)}]_0$ in Eq. (22) with Eq. (21),

$$[Y_{(total)}]_t = \frac{\theta}{\frac{\Gamma_{\infty(Y)}}{\delta} \cdot K_{eq}^Y \cdot k_{rxn}^{srf} + K_{eq}^Y \cdot \theta} \cdot W\left\{\frac{\frac{\Gamma_{\infty(Y)}}{\delta} \cdot K_{eq}^Y \cdot k_{rxn}^{srf} + K_{eq}^Y \theta}{\theta}[Y_{(total)}]_t^{blk} \cdot N_3\right\}$$

$$N_3 = exp\left(\frac{\frac{\Gamma_{\infty(Y)}}{\delta} \cdot K_{eq}^Y \cdot k_{rxn}^{srf} + K_{eq}^Y \theta}{\theta}[Y_{(total)}]_t^{rd} - \frac{\left(\frac{k_{diff}^{gas} \cdot \frac{\Gamma_{\infty(X)}}{\delta} \cdot k_{ads}}{k_{diff}^{gas} + \frac{\Gamma_{\infty(X)}}{\delta} \cdot k_{ads}}\right) \cdot \frac{\Gamma_{\infty(Y)}}{\delta} \cdot K_{eq}^Y \cdot k_{rxn}^{srf} \cdot S \cdot [X_{(g,\infty)}]}{\theta} \cdot \frac{V_{srf}}{V_{total}} \cdot t\right),$$

11

where $\boldsymbol{\theta}$ is defined as in Eq. (22). While it is clear these equations are cumbersome, we show in Sect. VI.B that they faithfully approximate the full numerical solutions of Eqs. (15)-(20). For further discussion on the approximations and assumptions made in obtaining Eqs. (21)-(23), see Sect. SI-2 of the Supplementary Information.

The steady state expressions for $[X_{(ads)}]$, $[X_{(rd)}]$, and $[X_{(core)}]$ derived in Sect. SI-2 and discussed above are substituted into the uptake equations (Eqs. (7)-(9)) to obtain the following expression for γ_{surf}, γ_{rd}, and γ_{core},

$$\gamma_{surf} = \frac{4\,r\,k_{rxn}^{srf}}{3\cdot\bar{c}} \cdot \left(\frac{k_{diff}^{gas} \cdot \frac{\Gamma_{\infty(X)}}{\delta} \cdot k_{ads}}{k_{diff}^{gas} + \frac{\Gamma_{\infty(X)}}{\delta} \cdot k_{ads}} \right) \frac{[Y_{(ads)}]}{\phi} \cdot \frac{V_{srf}}{V_{total}},$$

Eq. (24)

$$\gamma_{rd} = \frac{4\,r\,k_{rxn}^{blk}}{3\,\bar{c}} \frac{k_{Xdiff}^{rd} \cdot k_{Xsolv} \left(\frac{k_{diff}^{gas} \cdot \frac{\Gamma_{\infty(X)}}{\delta} \cdot k_{ads}}{k_{diff}^{gas} + \frac{\Gamma_{\infty(X)}}{\delta} k_{ads}} \right) \frac{[Y_{(total)}]}{\phi}}{\frac{\Gamma_{\infty(X)}}{\delta} \cdot k_{Xdesolv} \cdot k_{Xdiff}^{rd} + \frac{\Gamma_{\infty(X)}}{\delta} \cdot k_{Xdesolv} \cdot k_{rxn}^{blk}[Y_{(total)}] + k_{Xdiff}^{sb} \cdot k_{rxn}^{blk}[Y_{(total)}]} \cdot \frac{V_{rd}}{V_{total}},$$

Eq. (25)

$$\gamma_{core} = \frac{4\,r\,k_{rxn}^{blk}}{3\,\bar{c}} \frac{k_{Xdiff}^{core}\,k_{Xdiff}^{rd}\,H_{cc}^{gb}\,[Y_{(total)}]}{(k_{Xdiff}^{core} + k_{rxn}^{blk}[Y_{(total)}]) \cdot (k_{Xdiff}^{rd} + k_{rxn}^{blk}[Y_{(total)}])} \cdot \frac{V_{core}}{V_{total}},$$

Eq. (26)

where,

$$\boldsymbol{\phi} = k_{des} + k_{Xsolv} + [Y_{(ads)}]k_{rxn}^{srf} - \left(\frac{k_{des} \cdot \frac{\Gamma_{\infty(X)}}{\delta} k_{ads}}{k_{diff}^{gas} + \frac{\Gamma_{\infty(X)}}{\delta} k_{ads}} \right) - \left(\frac{k_{Xsolv} \cdot \frac{\Gamma_{\infty(X)}}{\delta} k_{Xdesolv}}{k_{Xdiff}^{sb} + \frac{\Gamma_{\infty(X)}}{\delta} k_{Xdesolv}} \right) -$$

$$\left(\frac{k_{Xdiff}^{sb} \cdot k_{Xdiff}^{rd} \cdot \frac{\Gamma_{\infty(X)}}{\delta} k_{Xdesolv} \cdot k_{Xsolv}}{\left(k_{Xdiff}^{rd} + \frac{\Gamma_{\infty(X)}}{\delta} k_{Xdesolv} \right) \times \left(\frac{\Gamma_{\infty(X)}}{\delta} k_{Xdesolv}[Y_{(total)}]\,k_{rxn}^{blk} + k_{Xdiff}^{sb}[Y_{(rd)}]k_{rxn}^{blk} + k_{Xdiff}^{rd} \cdot \frac{\Gamma_{\infty(X)}}{\delta} k_{Xdesolv} \right)} \right).$$

Eq. (27)

$[Y_{(ads)}]$ in Eq. (24) is computed using the Langmuir equation as described in Sect. V.C. Although lengthy, these expressions are general and account for cases where trace gas uptake is limited by either gas or liquid phase diffusion, or when there is strong coupling between surface and bulk reactions. Importantly, these expressions link the macroscopic quantity of an uptake coefficient (i.e., the fraction of collisions that yield a reaction) with the microscopic elementary steps of gas accommodation, reaction and diffusion. We note that Eq. (26) expressing uptake due to reaction in

12

the inner droplet core assumes that the interfacial X species denoted by *(ads)* and *(sb)* are equilibrated with the gas phase and equal to $H_{cc}^{gb}[X_{g,\infty}]$. This assumption is especially valid for the core uptake since for this reactivity to have much significance, the reacto-diffusive length must be on the order of the droplet radius, in which case the droplet interface is virtually in equilibrium with the gas phase. As we have shown previously,[10, 12, 20] these uptake expressions become much simpler for limiting cases often encountered in the laboratory. In Sect. VI we validate these closed form expressions against the numerical solutions to Eqs. (15)-(20) as well as prior experimental data on multiphase ozone kinetics in microdroplets.

V. Determination of Rate Coefficients

Here we summarize how to derive, compute or obtain each rate coefficient used in Eqs. (15)-(20) and the closed form expressions, Eqs. (21)-(27).

A. Gas Phase Diffusion of X: (k_{diff}^{gas})

The transport equation describing the diffusion of X to the boundary of a sphere of radius r is,[31]

$$J_c \left(\frac{molec}{s} \right) = 4\,\pi\,\cdot D_{gas}^X\,r\cdot \left[X_{(g,\infty)}\right], \qquad \text{Eq. (28)}$$

where D_{gas}^X is the gas phase diffusion constant of X. Here, J_c is the molecular flow in the "continuum" regime. We implement diffusion in the model as two reversible steps described by a rate coefficient,

$$\left[X_{(g,\infty)}\right] \underset{k_{diff}^{gas}}{\overset{k_{diff}^{gas}}{\rightleftarrows}} \left[X_{(gs)}\right], \qquad \text{(R1)}$$

where k_{diff}^{gas} is obtained by analyzing the origin of transport equation Eq. (28) and normalizing J_c by a relevant volumetric term and the gas concentration $[X_{(g,\infty)}]$.

J_c is derived using the expression for diffusion of species X through a spherical wall with outer boundary b and inner boundary a as provided by Crank:[32]

$$J_c \left(\frac{molec}{s} \right) = 4\,\pi\cdot D_{gas}^X\,\frac{b\cdot a}{b-a}\cdot ([X_b] - [X_a]), \qquad \text{Eq. (29)}$$

13

where the inner boundary $a = r$ and the concentrations are chosen to be $[X_b] = [X_{g,\infty}]$ and $[X_a] = 0$. Setting $[X_a] = 0$ in this way provides the upper bound for the rate of diffusive transport where the surface concentration at r is completely depleted. For the outer boundary b, we consider the limit $b \to \infty$ to identify a limiting value for J_c where the flow of X to the spherical interface approaches a minimum. In the limit $b \to \infty$, Eq. (29) becomes,

$$J_c \left(\frac{molec}{s}\right) = 4\,\pi \cdot D_{gas}^X\, r \cdot [X_{(g,\infty)}], \qquad \text{Eq. (30)}$$

which is equivalent to Eq. (28). This expression is divided by the spherical shell volume of the surface to obtain a rate equation,

$$Rate\left(\frac{molec}{cm^3\,s}\right) = \frac{J_c}{V_{srf}} = \frac{4\pi\,D_{gas}^X\,r}{\frac{4}{3}\pi\,(r^3 - (r-\delta)^3)} \cdot [X_{(g,\infty)}] \approx \frac{4\pi\,D_{gas}^X\,r}{4\pi\,r^2\,\delta} \cdot [X_{(g,\infty)}], \qquad \text{Eq. (31)}$$

where the surface volume can be approximated by the product of the spherical surface area and surface thickness δ when $r \gg \delta$. From Eq. (31), the rate of diffusion to the interface is,

$$Rate\left(\frac{molec}{cm^3\,s}\right) = k_{diff}^{gas} \cdot [X_{(g,\infty)}] \qquad \text{Eq. (32)}$$

where the gas-diffusion rate coefficient is,

$$k_{diff}^{gas} = \frac{D_{gas}^X}{r\,\delta}. \qquad \text{Eq. (33)}$$

This rate coefficient controls both the diffusion rate of X into the surface compartment generating $[X_{(gs)}]$, but also the rate at which $[X_{(gs)}]$ diffuses away from the surface, re-generating $[X_{(g,\infty)}]$, as illustrated in Fig. 2. This rate of diffusion is inherently coupled to the rate at which X may adsorb to the interface. An understanding of this phenomenon and a comparison of the current treatment with previous derivations by Fuchs and Sutugin[33] is provided in Appendix A.

B. Trace Gas X Adsorption, Desorption, Solvation and Desolvation: (k_{ads}, k_{des}, k_{Xsolv}, $k_{Xdesolv}$)

Describing multiphase chemical kinetics requires accounting for both diffusion that governs larger-scale transport between two phases, and the adsorption/desorption terms in Fig. 2 that govern molecular-scale transport at an interface. First, we consider how the adsorption rate coefficient is related to the collision frequency of a gas X on the droplet interface. Appendix A

14

unites this gas kinetic framework with a diffusional picture and ties this relationship back to macroscopic gas-transport descriptions.

Once reactant X has diffused to the liquid surface, adsorption (*i.e.,* thermal accommodation) to the surface is described by a Langmuir model,[34] where adsorption occurs at specific sites (site$_X$),

$$X_{(gs)} + site_X \underset{k_{des}}{\overset{k_{ads}}{\rightleftharpoons}} X_{(ads)}.$$ (R2)
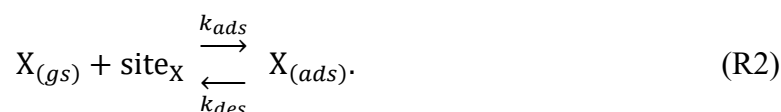
The maximum volumetric site concentration, $[site_X]_{max}$, is computed from the molecular area of X ($\frac{1}{\Gamma_{\infty(X)}}$, cm^2 molec.$^{-1}$) and the interface thickness ($\delta = 1$ nm),

$$[site_X]_{max} = \frac{\Gamma_{\infty(X)}}{\delta}.$$ Eq. (34)

k_{ads} is computed such that the pseudo-first order adsorption rate is consistent with the collision frequency obtained by a simple Maxwellian picture of molecular translation,

$$[site_X]_{max} \cdot k_{ads} = \sigma \cdot \frac{\bar{c}}{4\,\delta}\ ,$$ Eq. (35)

where $\bar{c}$ is the average velocity of X in the gas phase and σ the sticking coefficient. The desorption rate coefficient, k_{des} is related to the average molecular lifetime at the interface, $\tau = \frac{1}{k_{des}}$, which is on the order of ~10-100 ps for many low-molecular weight gases on water surfaces under ambient atmospheric conditions. These lifetimes can be obtained through a variety of theoretical and experimental techniques.[35] The elementary steps that describe solvation/desolvation of X into the liquid phase are described similarly,

$$X_{(sb)} + site_X \underset{k_{Xsolv}}{\overset{k_{Xdesolv}}{\rightleftharpoons}} X_{(ads)}.$$ (R3)
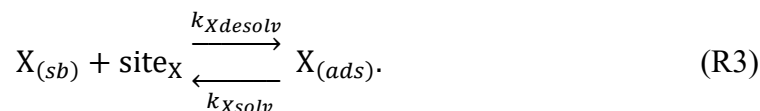
The Henry's law constant for X provides an important constraint for the rate coefficients in R2 and R3. The overall Henry's law coefficient for a gas dissolving into a bulk liquid (H_{cc}^{gb}) is a coupled equilibrium,[11, 12, 20, 36, 37] which links gas, interface and bulk concentrations of X,

$$H_{cc}^{gs} = \frac{k_{ads}\,[site_X]}{k_{des}},$$ Eq. (36)

15

$$H_{cc}^{sb} = \frac{k_{Xsolv}}{k_{Xdesolv} \cdot [\text{site}_X]}, \qquad \qquad \text{Eq. (37)}$$

where,

$$H_{cc}^{gb} = H_{cc}^{gs} \cdot H_{cc}^{sb} \qquad \qquad \text{Eq. (38)}$$

and,

$$H_{cc}^{gb} = \frac{k_{ads}}{k_{des}} \cdot \frac{k_{Xsolv}}{k_{Xdesolv}}. \qquad \qquad \text{Eq. (39)}$$

These "partial" Henry's law coefficients (Eqs. (36) and (37)) are conceptually useful since the concentration of a X at the interface may be significantly different than both the gaseous and liquid-phase concentrations at equilibrium as illustrated in Fig. 1. Furthermore, they provide through Eqs. (36)-(39) an expression that links the forward and backward rate coefficients for adsorption, desorption, solvation and desolvation to the Henry's law equilibrium constants. Although this constrains the ratios for solvation and adsorption (*i.e.*, $\frac{k_{Xsolv}}{k_{Xdesolv} \cdot [\text{site}_X]}$ and $\frac{k_{ads}[\text{site}_X]}{k_{des}}$), further information is needed to obtain the absolute values for k_{ads}, k_{des}, k_{Xsolv} and $k_{Xdesolv}$. H_{cc}^{gs}, H_{cc}^{sb}, k_{des}, and k_{Xsolv} can be obtained from potential of mean force calculations[21] and associated trajectories in MD simulations[10-12, 20, 38] thus constraining the values of k_{ads}, and $k_{Xdesolv}$.

Example Calculation O₃ uptake onto microdroplets: Here we provide a concrete example from our recent work[10, 20, 38] that illustrates how k_{ads}, k_{des}, k_{Xsolve}, and $k_{Xdesolv}$ are determined. From prior MD simulations for O$_3$ at the air-water interface:[20] $H_{cc}^{gs} = 4.97$ and $k_{des} = 1.93 \times 10^{10}\ s^{-1}$. As computed by Vieceli *et al.*,[22] the molecular area ($\frac{1}{\Gamma_{\infty(X)}}$) for ozone is 1.85 nm^2, which corresponds to a volumetric density at the interface of $\frac{\Gamma_{\infty(X)}}{\delta} = 5.42 \times 10^{21}$ site/cm^3. This yields,

$$k_{ads} = k_{des} \cdot H_{cc}^{gs} \cdot \frac{\delta}{\Gamma_{\infty(X)}} = 1.77 \times 10^{-11}\ \text{cm}^3/\text{molecule s}^{-1}. \qquad \text{Eq. (40)}$$

$$k_{ads} \cdot \frac{\Gamma_{\infty(X)}}{\delta} = k_{des} \cdot H_{cc}^{gs} = 9.59 \times 10^{10}\ \text{s}^{-1}, \qquad \text{Eq. (41)}$$

16

An alternative way to compute k_{ads} is from gas kinetic theory. The flux of O_3 onto the droplet surface can be computed by dividing the molecular flow J_k (see Appendix A) by the droplet area to give,

$$Flux \left(\frac{molec}{cm^2\ s}\right) = \frac{J_k}{4\pi r^2} = \frac{\bar{c}}{4} \cdot \left[O_{3(g,\infty)}\right]. \qquad \text{Eq. (42)}$$

The flux expression Eq. (42) is augmented to define a rate of O_3 entering the interfacial volume of the liquid by multiplying the flux by the surface-to-volume ratio of the interfacial compartment,

$$Rate \left(\frac{molec}{cm^3\ s}\right) = Flux \cdot \frac{4\pi r^2}{4\pi r^2 \cdot \delta} = \frac{\bar{c}}{4 \cdot \delta} \cdot \left[O_{3(g,\infty)}\right]. \qquad \text{Eq. (43)}$$

The first (k_{col}^{1st}) and second-order (k_{col}^{2nd}) collision rate coefficients are,

$$k_{col}^{1st} = k_{col}^{2nd} \cdot \frac{\Gamma_{\infty(X)}}{\delta} = \frac{\bar{c}}{4 \cdot \delta} \qquad \text{Eq. (44)}$$

Using $\frac{\Gamma^\infty}{\delta} = 5.42 \times 10^{21}$ site/cm^3, the rate coefficients in Eq. (44) are,

$$k_{col}^{2nd} = \frac{\bar{c}}{4 \cdot \Gamma_{\infty(X)}} = 1.66 \times 10^{-11} \text{ cm}^3 \text{ molecule}^{-1} \text{ s}^{-1}, \qquad \text{Eq. (45)}$$

$$k_{col}^{1st} = 9 \times 10^{10} \text{ s}^{-1}. \qquad \text{Eq. (46)}$$

For the case where adsorption of X occurs on every collision (*i.e.*, σ =1, $k_{ads} = \sigma \cdot k_{col}$). Eq. (44) is equivalent to $k_{ads} \cdot \frac{\Gamma_{\infty(X)}}{\delta}$. From k_{ads} and H_{cc}^{gs}, k_{des} is computed via Eq. (36). The values of k_{ads} obtained by constraining k_{des} via MD simulations (Eqs. (40) and (41)) or alternatively using gas kinetic theory (Eqs. (45) and (46)) differ by only ~ 5%. This difference likely originates from assumptions made in defining $\Gamma_{\infty(X)}$ and δ. The way in which the adsorption dynamics at the interface are coupled with the diffusional dynamics of gas transport to the interface is explored in detail in Appendix A.

k_{Xsolv} is directly obtained from MD simulations or coarse grain dynamics using the Fokker–Planck equation.[38] The solvation rate of thermalized O_3 at the air-water interface is k_{Xsolv}= 1.9x10^8 s^{-1}.[38] For reference the mass accommodation coefficient[38] ($\alpha = k_{Xsolv}/(k_{des} + k_{Xsolv})$.) obtained from MD simulations is α = 9.7 x 10^{-3}. From Eq. (33) and $\frac{\Gamma_{\infty(X)}}{\delta}$, $k_{Xdesolv}$= 2.25 x 10^{-12} cm^3 molec.$^{-1}$ s^{-1} in this example.

C. Surface Partitioning of Solute Y (K_{eq}^Y, $k_{Ydesolv}$, k_{Ysolv})

The partitioning of the non-volatile solute Y to and from the interface is described in two elementary steps using a Langmuir adsorption model,

$$Y_{(sb)} + site_Y \underset{k_{Ysolv}}{\overset{k_{Ydesolv}}{\rightleftarrows}} Y_{(ads)} \tag{R4}$$
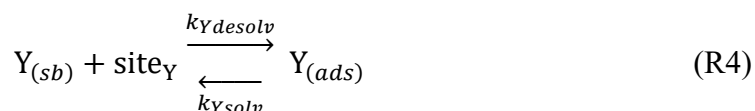
where $[Y_{(ads)}]$ is,

$$[Y_{(ads)}] = [site_Y]_{max} \frac{K_{eq}^Y \cdot [Y_{(bulk)}]}{1 + K_{eq}^Y \cdot [Y_{(bulk)}]} \tag{Eq. (47)}$$

and,

$$K_{eq}^Y = \frac{k_{Ydesolv}}{k_{Ysolv}} \tag{Eq. (48)}$$

and,

$$[site_Y]_{max} = \frac{\Gamma_{\infty(Y)}}{\delta}. \tag{Eq. (49)}$$

We note that while adsorption of Y is described in step (R4) by the near-interfacial species $Y_{(sb)}$, in the current model this is equivalent to the adsorption of $Y_{(total)}$ since we have assumed instantaneous mixing of species Y throughout the droplet and hence, not formally distinguished species $Y_{(sb)}$, $Y_{(rd)}$, and $Y_{(core)}$. The Langmuir equilibrium constant (K_{eq}^Y) is analogous to H_{cc}^{sb} for X described above (Eq. (37)). Values K_{eq}^Y and $\Gamma_{\infty(Y)}$ can be obtained by a number of experimental and theoretical methods. Static and dynamic surface tension measurements are used to obtain values of K_{eq}^Y, $\Gamma_{\infty(Y)}$, k_{Ysolv} and $k_{Ydesolv}$. For example, Bleys and Joos[39] found that for small acids and alcohols values of k_{Ysolv} were all around ~ 100 s^{-1}, whereas values of $k_{Ydesolv}$ varied by orders of magnitude and depend upon molecular structure. Nonlinear optical studies of air-water interfaces[40] can also constrain values of K_{eq}^Y through determinations of the Gibbs Adsorption free energy. Furthermore, MD simulations provide density profiles of solutes at the air-water interface that can constrain K_{eq}^Y. We note that all these determinations generally rely on model assumptions within a Langmuir framework, the consequences of which have been discussed elsewhere.[40-42]

D. Liquid Phase Diffusion of X: (k_{Xdiff}^{sb}, k_{Xdiff}^{rd}, k_{Xdiff}^{core})

In addition to the microscopic kinetic steps that describe solvation and desolvation described above, a diffusional description is used to describe the larger-scale transport of X and Y in the liquid phase. As shown below for the species X, we formulate liquid phase diffusion in a way that is analogous to a kinetic rate law. This description follows the same method used in Kinetiscope©[13] to calculate diffusion between two adjacent compartments.

The diffusive flux between two compartments from Fick's First Law is,

$$Flux\left(\frac{molec.}{cm^2 \cdot s}\right) = -D^X_{liquid} \nabla[X] = -D^X_{liquid} \frac{([X_1]-[X_2])}{\frac{1}{2} \cdot (L_1+L_2)}, \qquad \text{Eq. (50)}$$

where $[X_1]$ and $[X_2]$ are the concentrations of X in compartments 1 and 2, respectively. L_1 and L_2 refer to the lengths of the respective, adjacent compartments (*e.g.,* δ and L_{rd} or L_{rd} and L_{core}) and D^X_{liquid} is the liquid phase diffusion constant of X. Multiplying Eq. (50) by the cross-sectional area *A* between the two compartments gives an expression for the molecular flow, or the number of molecules transferred per second,

$$Flow\left(\frac{molec.}{s}\right) = -2 \cdot D^X_{liquid} \cdot \frac{([X_1]-[X_2])}{(L_1+L_2)} \cdot A. \qquad \text{Eq. (51)}$$

Dividing Eq. (51) by a volume yields a rate equation,

$$Rate\left(\frac{molec.}{s\,cm^3}\right) = -2 \cdot D^X_{liquid} \cdot \frac{([X_1]-[X_2])}{(L_1+L_2)} \cdot \frac{A}{V} \qquad \text{Eq. (52)}$$

where *V* corresponds to either compartment 1 or 2 (i.e., $V_1 = A\,L_1$ or $V_2 = A\,L_2$), and depends upon the specific process considered. As shown below, the choice of *V* is determined by which process Eq. (52) is intended to describe.

To fully describe diffusion between two adjacent compartments, four kinetic steps are required as outlined in the two processes in Fig. 3.

19
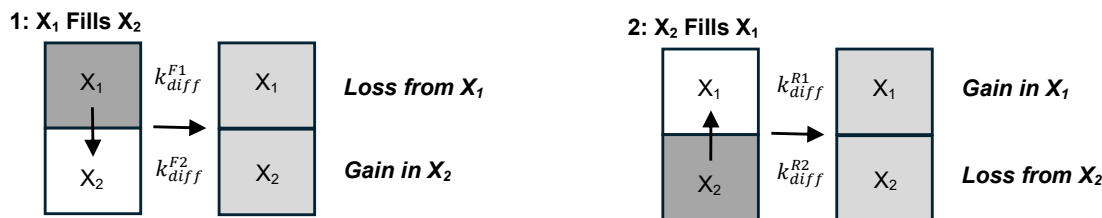
Figure 3: Liquid diffusion between two compartments shown schematically as two elementary processes. In (1, left panel), X moves from compartment 1 to compartment 2 and species X_1 is lost (at a rate proportional to coefficient k_{diff}^{F1}) to produce X_2 (at a rate proportional to coefficient k_{diff}^{F2}). In (2, right panel), the reverse process is shown with proportional constants k_{diff}^{R1} and k_{diff}^{R2}.

In actuality, the two processes illustrated in Fig. 3 occur simultaneously as the system equilibrates. Regardless of the initial conditions, the rate equations for concentrations $[X_1]$ and $[X_2]$ are,

$$\frac{d[X_1]}{dt} = k_{diff}^{F1}[X_1] + k_{diff}^{R1}[X_2], \qquad \text{Eq. (53)}$$

$$\frac{d[X_2]}{dt} = k_{diff}^{R2}[X_2] + k_{diff}^{F2}[X_1]. \qquad \text{Eq. (54)}$$

To calculate a specific term (*e.g.* k_{diff}^{F1}) we use Eq. (52) and assuming $[X_2] = 0$,

$$k_{diff}^{F1}[X_1] = Rate = -2 \cdot D_{liquid}^{X} \cdot \frac{([X_1]-0)}{(L_1+L_2)} \cdot \frac{A}{V_1}, \qquad \text{Eq. (55)}$$

where,

$$k_{diff}^{F1} = -\frac{2 \cdot D_{liquid}^{X}}{(L_1+L_2) \cdot L_1}. \qquad \text{Eq. (56)}$$

Importantly, V_1 is selected as the relevant volume in Eq. (55) since the coefficient in question k_{diff}^{F1} is defined by the derivative in Eq. (53) and represents the concentration change of X within V_1.

Following the same derivation for k_{diff}^{R1} yields,

$$k_{diff}^{R1}[X_2] = Rate = -2 \cdot D_{liquid}^{X} \cdot \frac{(0-[X_2])}{(L_1+L_2)} \cdot \frac{A}{V_1}, \qquad \text{Eq. (57)}$$

$$k_{diff}^{R1} = \frac{2 \cdot D_{liquid}^{X}}{(L_1+L_2) \cdot L_1} = -k_{diff}^{F1}. \qquad \text{Eq. (58)}$$

20

This shows that within a given differential, *e.g.* Eq. (53), the forward and reverse diffusion rate coefficients are equal in magnitude and opposite in sign. Similarly, the forward and reverse rate constants in the differential for compartment 2 in Eq. (54) are,

$$k_{diff}^{R2} = -\frac{2 \cdot D_{liquid}^X}{(L_1 + L_2) \cdot L_2} = -k_{diff}^{F2}, \qquad \text{Eq. (59)}$$

which is obtained using the same procedure albeit using V_2 instead.

Using this formalism, the specific equations that govern the liquid phase diffusion rate of $X_{(sb)}$ and $X_{(rd)}$ shown in Fig. 2 are,

$$\frac{d[X_{(sb)}]}{dt} = -k_{Xdiff}^{sb}[X_{(sb)}] + k_{Xdiff}^{sb}[X_{(rd)}], \qquad \text{Eq. (60)}$$

$$\frac{d[X_{(rd)}]}{dt} = -k_{Xdiff}^{rd}[X_{(rd)}] + k_{Xdiff}^{rd}[X_{(sb)}], \qquad \text{Eq. (61)}$$

where,

$$k_{Xdiff}^{sb} = \frac{2 \cdot D_{liquid}^X}{(L_{rd} + \delta) \cdot \delta} \qquad \text{Eq. (62)}$$

$$k_{Xdiff}^{rd} = \frac{2 \cdot D_{liquid}^X}{(L_{rd} + \delta) \cdot L_{rd}} \qquad \text{Eq. (63)}$$

$$k_{Xdiff}^{core} = \frac{2 \cdot D_{liquid}^X}{r \cdot (r - L_{rd})} \qquad \text{Eq. (64)}$$

Eq. (64), the diffusion rate into the core, is obtained using the methods outlined above. This same formalism can be applied to represent the diffusion rate of Y to and from the liquid interface. This case is not explicitly considered in the derivations shown above since we have broadly assumed the mixing time for species Y to be much faster than the reaction. However, for cases where depletion of Y near the interface is possible, an additional set of rates equations can be used, as we will demonstrate in future work.

## E. Surface and Bulk Reaction Rate Coefficients: $\left(k_{rxn}^{srf}, k_{rxn}^{blk}\right)$

The surface and bulk rate coefficients for the X + Y reaction are key quantities for predicting multiphase reaction kinetics. Bulk rate coefficients used in this multiphase model are usually obtained from beaker-scale experiments or theoretical calculations usually under dilute

21

conditions. As illustrated in Fig. 2, linking reactivity in beaker scale solutions of X and Y with the analogous multiphase reaction requires understanding all of the non-reactive steps that govern the partitioning of X and Y between various phases (i.e., gas, interface, and bulk). In previous models[12] using a similar framework, we generally assume (in the absence of evidence to the contrary) that the surface reaction rate coefficient is equivalent to the bulk (*i.e.,* $k_{rxn}^{srf} = k_{rxn}^{blk}$). However, there are good reasons to expect that this might not always be the case since the partial solvation at an interface can lower reaction barriers or induce more favorable molecular orientations for a reaction to occur. For example, recent work suggests that rate coefficients for condensation reactions are 100-10000 times faster at air-water and oil-water interfaces than in bulk solutions.[43-46] Furthermore, as demonstrated recently by comparing model predictions and experiments, surface rate coefficients can be estimated for those cases where the partitioning of X and Y between phases can be adequately constrained.[8, 10, 44]

VI. Model Validation with Experimental Measurements

A. Numerical Solutions

Eqs. (15)-(20) are numerically solved and compared to previously published experimental kinetic measurements for three different systems. For this comparison, O_3 oxidation reactions are analyzed on levitated microdroplets. The oxidation kinetics of aqueous droplets of maleic acid (MA),[47] nitrite (NO_2^-),[48] and iodide (I^-)[10, 20] are selected to illustrate a number of different

22
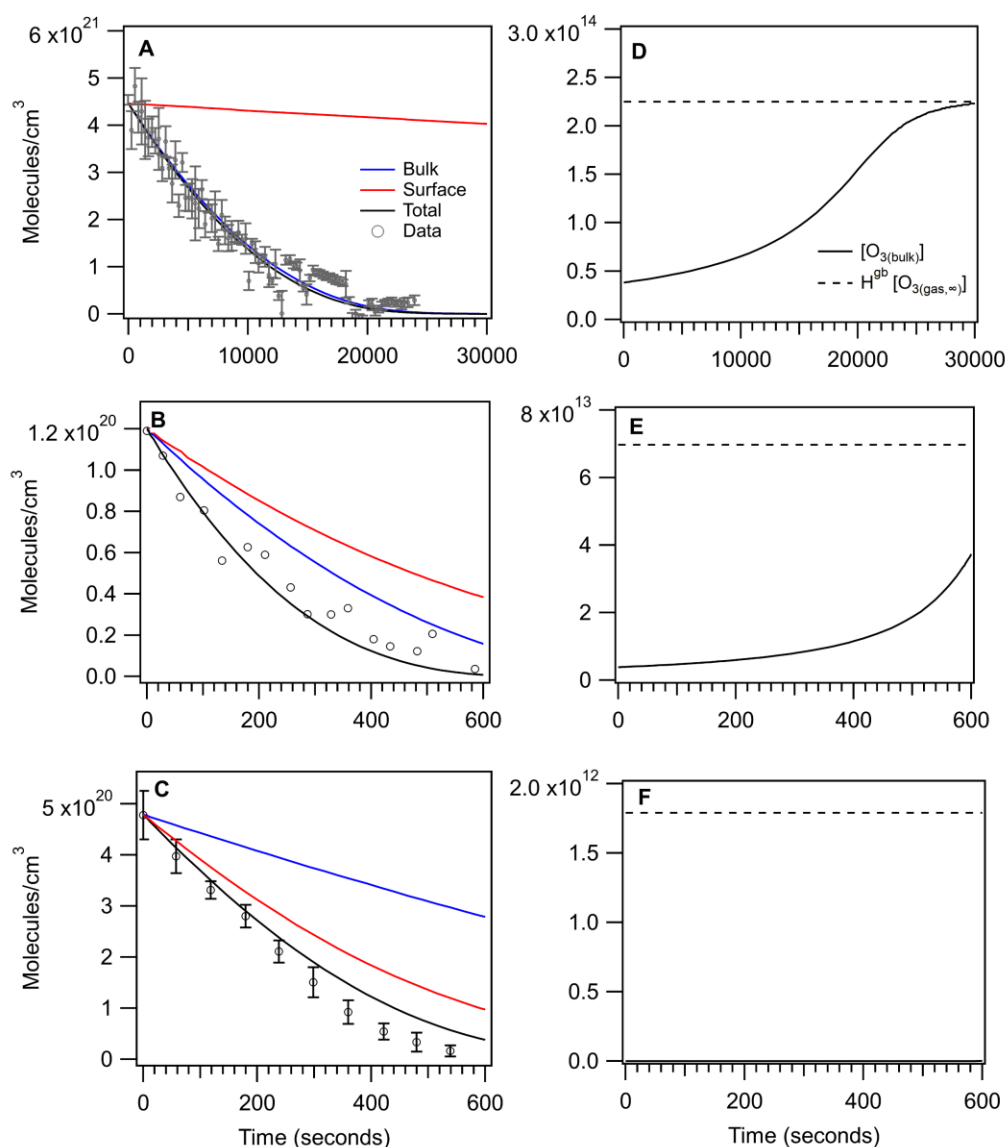
Figure 4: Kinetic model results compared to measurements for three reactive systems. The left column shows kinetics for the ozone oxidation of aqueous (A) maleic acid, (B) nitrite and the (C) iodide. Model results include the full model in black (*i.e.,* total = surface and bulk) along with the bulk-only model (bulk = *rd* and *core*) in blue and the surface-only model in red. The right column (D-F) shows for each the predicted time-dependent of $[O_{3(bulk)}]$ in the droplet. See Table SI for a complete set of experimental and model parameters.

scenarios. These reactants span a large range of reactivities with ozone, with aqueous rate coefficients (see Table S1) ranging from $k = 1.7 \times 10^3$ M^{-1} s^{-1} for MA to $k = 3.4 \times 10^5$ M^{-1} s^{-1} for NO$_2^-$ and $k = 1.2 \times 10^9$ M^{-1} s^{-1} for I$^-$. For each reaction, numerical solutions to the Eqs. (15)-(20)

23

are obtained using the ND solve algorithm in *Mathematica*,[49] with the output compared to experimental results shown in Fig. 4. Table S1 in the Supplementary Information provides the relevant experimental conditions and coefficients used for each reaction. References for and a discussion of the values in Table S1 can be found in Sec. SI-3.

To highlight the relative roles of the surface and bulk reaction for each case shown in Fig. 3, the full set of Eqs. (15)-(20) is evaluated and labeled "total" in Fig. 4. Total includes surface and bulk (*rd* and *core*) reactions In each case, the numerical predictions replicate the observed decay kinetics for maleic acid, nitrite and iodide. To ascertain the surface and bulk contributions to the total observed kinetics, a modified set of predictions are shown in Fig. 4, where only surface reactions (labeled "surface") and only the bulk reactions (labeled "bulk") are computed. The "surface" set is computed by removing all terms with k_{rxn}^{blk} from Eq. (15)-(20) and the "bulk" is computed by removing terms with k_{rxn}^{srf}. This comparison demonstrates that the maleic acid reaction is predicted to have only a minor surface contribution, whereas the nitrite and iodide reactions display comparable reactive contributions from both the surface and the bulk. Due to the differences in the nitrite and iodide reactivities and surface propensities, however, the bulk reaction is slightly more favored in the case of NO_2^- whereas the surface is for I^-. We note that in previous studies, which did not include an explicit *rd* compartment, we underestimated the contribution of the bulk reaction to the multiphase kinetics of nitrite.[11, 12]

The right column in Fig. 4 shows the time-evolution of O_3 within the droplet. This concentration is a weighted sum of the O_3 concentration within the reactive-diffusion region and the core region, providing an average concentration throughout the entire droplet. For each system, O_3 is significantly depleted relative to its Henry's law value ($H_{cc}^{gb} = [X_{(g,\infty)}]$), unlike "phase-mixed" kinetics which dominate for much slower reactions.[27] For the MA reaction, $[O_3]$ recovers to its Henry's law value during the reaction. For the faster rates of nitrite and iodide, ozone remains depleted throughout the entire reaction, with a moderate recovery observed in the NO_2^- reaction and virtually no recovery for the I^- case. Intuitively, the degree of O_3 depletion scales with the reaction-diffusion length of ozone at a given time, with severe depletion occurring for scenarios where the reaction-diffusion length is significantly smaller than the droplet radius throughout the reaction.

B. Evaluation of the Closed Form Expressions

24

The closed form expression in Eq. (23) is used to calculate the time-dependence of iodide loss from the example discussed above. Predictions of Eq. (23) are compared in Fig. 5 with the exact numerical solutions and the experimental iodide data shown in Fig. 4. We also include
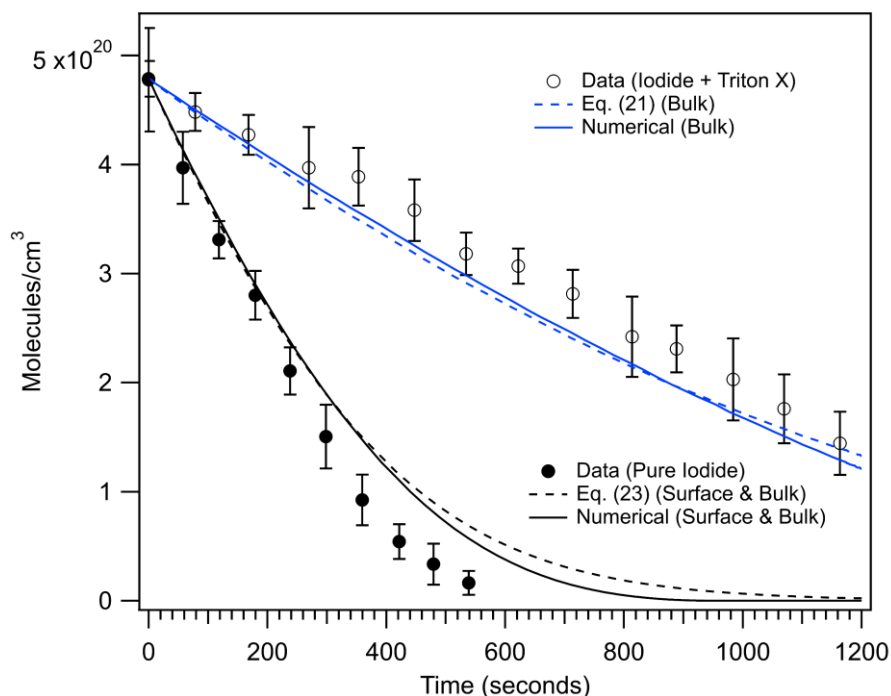
Figure 5: Closed form time-dependent expressions for $[I^-]_t$ calculated using Eq. (23) (total) and Eq. (21) (bulk reaction only). Analytical expressions are compared to the numerical evaluations described above and shown in Fig. 4. Two sets of experimental kinetics are included here, the first for the standard $I^- + O_3$ reaction (●) shown in Fig. 3, and another set including 1.6 mM of Triton-X100 (○). The presence of the surfactant completely inhibits the surface reaction in this case, demonstrated by agreement with the bulk-only models. For both sets of kinetics, $[O_{3(g,\infty)}] = 500$ ppb, $r = 17$ um, and $[I^-]_0 = 795$ mM.

predictions of the "bulk" only (i.e., rd compartment) closed form expression (Eq. (21)) and compare it with measurements of $O_3 + I^-$ reaction in the presence of surfactant Triton-X 100,[50] which effectively shuts off the surface reaction. The comparison shown in Fig. 5 confirms that the closed form expressions closely replicate both the experimental data and the numerical solutions, and thus validates the approximations used in deriving these analytic functions.

VI. Conclusions

The general approach described above establishes a framework for evaluating multiphase chemical kinetics. Unlike previous models (see review by Kolb *et al.*[51] and discussion in Wilson

25

et. al.[12]), which use flux-based descriptions, our approach seeks to distill multiphase chemistry into a simple set of physically realistic elementary kinetic steps and equilibria. This kinetic description incorporates the interfacial dynamics and solvation free energies observed in MD simulations as well as continuum descriptions of mass transport. The resulting set of differential equations and expressions for uptake are embedded in a coarse grain description of kinetically relevant spatial regions in a two-phase system. The simple set of coupled differential equations, which when solved numerically or analytically, produce predictions that can be directly compared to experimental observations. The model provides a novel way to evaluate the contribution of interfacial and bulk phase reactions to uptake coefficients and the overall reaction kinetics, thus providing deeper insight into the multiphase mechanism, which is often not possible when considering experimental results alone. This framework appears to be general and likely transferrable to, for example, problems involving the transport of solutes across electrolyte/membrane interfaces or chemical reactions in coacervates.[52]

Appendix A: Molecular and Continuum Descriptions of Gas Diffusion to an Interface

In the kinetic model described above we derive expressions that account for the diffusive and kinetic mass transfer of X to the gas-liquid surface. The rate equation describing diffusional transport is,

$$Rate\left(\frac{molec}{cm^3\,s}\right) = \frac{J_c}{V_{srf}} = k_{diff}^{gas} \cdot \left[X_{(g,\infty)}\right] \qquad \text{Eq. (A1)}$$

where J_c indicates the molecular flow in the "continuum" regime as previously defined in Eq. (30),

$$J_c\left(\frac{molec}{s}\right) = 4\,\pi \cdot D_{gas}^X\,r \cdot \left[X_{(g,\infty)}\right], \qquad \text{Eq. (A2)}$$

which is transformed into a first-order rate coefficient by normalizing by the approximate surface volume $4\pi r^2\,\delta$ and gas concentration (see Sect. V.A):

$$k_{diff}^{gas}(s^{-1}) = \frac{D_{gas}^X}{r\,\delta}. \qquad \text{Eq. (A3)}$$

The analogous rate equation describing kinetic or "collisional" mass transport to the interface is,

$$Rate\left(\frac{molec}{cm^3\,s}\right) = \frac{J_k}{V_{srf}} = k_{col} \cdot \left[X_{g,\infty}\right] \qquad \text{Eq. (A4)}$$
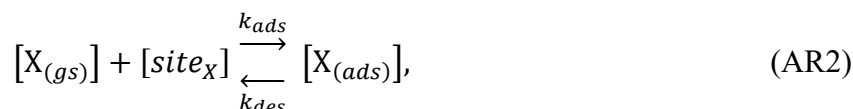
26

where J_k indicates the molecular flow in the kinetic regime,

$$J_k \left(\frac{molec}{s} \right) = 4 \pi r \frac{\bar{c}}{4} \cdot \left[X_{(g,\infty)} \right], \qquad \text{Eq. (A5)}$$

which is similarly recast as a first-order rate coefficient by normalizing by the approximate surface volume:

$$k_{col}(s^{-1}) = \frac{\bar{c}}{4 \, \delta}. \qquad \text{Eq. (A6)}$$

Written out in kinetic steps, we describe the overall process using two reversible steps,

$$\left[X_{(g,\infty)} \right] \underset{k_{diff}^{gas}}{\overset{k_{diff}^{gas}}{\rightleftarrows}} \left[X_{(gs)} \right], \qquad \text{(AR1)}$$

$$\left[X_{(gs)} \right] + [site_X] \underset{k_{des}}{\overset{k_{ads}}{\rightleftarrows}} \left[X_{(ads)} \right], \qquad \text{(AR2)}$$

where $site_X$ denotes a surface site for X, with maximum coverage given by Γ_X^∞ / δ as previously discussed. The collision rate coefficient k_{col} is equal to the pseudo-first order adsorption rate $k_{col} = k_{ads} \frac{\Gamma_X^\infty}{\delta}$, assuming $\sigma = 1$ (see Sect. V.B).

During the net-adsorption process the diffusional transport (AR1) described above and the interfacial adsorption process (AR2) occur simultaneously, and therefore, the concentration of near-surface species $\left[X_{(gs)} \right]$ has both diffusional and adsorption contributions to its steady-state value. In the limit of complete surface loss after surface adsorption, the steady-state concentration of $\left[X_{(gs)} \right]$ is,

$$\left[X_{gs} \right] = \frac{k_{diff}^{gas}}{k_{ads} \cdot \frac{\Gamma_X^\infty}{\delta} + k_{diff}^{gas}} \left[X_{(g,\infty)} \right] = \frac{\frac{D_{gas}^X}{r \, \delta}}{\frac{\bar{c}}{4 \, \delta} + \frac{D_{gas}^X}{r \, \delta}} \left[X_{(g,\infty)} \right] = \frac{J}{J_k} \left[X_{(g,\infty)} \right]. \qquad \text{Eq. (A7)}$$

Eq. (A7) denotes the "effective" concentration of X from the perspective of the interface. During adsorption and loss of X, the near-surface concentration $\left[X_{(gs)} \right]$ resembles $\left[X_{(g,\infty)} \right]$ when the radius r is small but becomes significantly depleted when r is large—since the loss of X due to interfacial adsorption becomes faster than what can be "replenished" by diffusional transport, which slows

27

with increasing r as seen in Eq. (A3). From an alternative point of view, Eq. (A7) expresses that the near-surface gas concentration is related to the true gas concentration by a transport fractional term that expresses how much the near-surface gas behavior resembles the "molecularity" expected by the purely collisional description used for adsorption. As included in Eq. (A7), this can be expressed by a simple ratio of flux terms, where the true gas flux (J) divided by a reference flux (the molecular flux J_k in this case) provides the fractional term.

This first observation is equivalent to that of Fuchs & Sutugin[33] using the method of flux-matching to a boundary sphere of radius $r + \Delta$ for the elementary case where $\Delta = 0$, expressed in terms of the Knudsen number $\text{Kn} = \frac{3\,D_{gas}^X}{\bar{c}\,r}$:

$$F_{\Delta=0}^k = \frac{J}{J_k} = \frac{1}{1+\frac{3}{4}\text{Kn}^{-1}}.$$ Eq. (A8)

Note that Eq. (A8) can instead be represented as the fraction of the diffusional flux rather than kinetic flux, which applies under the continuum regime where:

$$F_{\Delta=0}^c = \frac{J}{J_c} = \frac{1}{1+\frac{4}{3}\text{Kn}},$$ Eq. (A9)

given the relation

$$\frac{J_c}{J_k} = \frac{4}{3}\text{Kn}.$$ Eq. (A10)

Although the gas-transport term in Eq. (A7) and Fuchs' expression for $\Delta = 0$ agree exactly, the transport Eq. (A7) can be slightly modified to agree with Fuchs' general expression for a general boundary sphere of $r + \Delta$. To accomplish this, we set up a simple expression that is in fact equivalent to Fuchs' continuous description of boundary-sphere flux matching. We define a flux-matching boundary condition by recognizing that the number of molecules that diffuse from the gas phase into the near-surface region must equal the sum of the number of molecules colliding with the droplet surface and diffusing back out into the outer gas phase,

$$4\pi\,D_{gas}^X\,(r+\Delta)\big[X_{(g,\infty)}\big] = 4\pi\,D_{gas}^X\,(r+\Delta)\big[X_{(gs)}\big] + 4\pi\,r^2\frac{\bar{c}}{4}\big[X_{(gs)}\big],$$ Eq. (A11)

which can be rearranged to express the steady state concentration of near-surface gas concentration, analogous to Eq. (A7):

$$[X_{(gs)}] = \frac{4\pi\, D_{gas}^X\, (r + \Delta)}{4\pi\, r^2 \frac{\bar{c}}{4} + 4\pi\, D_{gas}^X\, (r + \Delta)} \left[X_{(g,\infty)}\right].$$

<div align="right">Eq. (A12)</div>

The gas-transport term in Eq. (A12) can be rearranged using the definition of the Knudsen number Kn to yield,

$$\frac{4\pi\, D_{gas}^X\, (r + \Delta)}{4\pi\, r^2 \frac{\bar{c}}{4} + 4\pi\, D_{gas}^X\, (r + \Delta)} = \frac{J}{J_k} = \frac{1 + \mathrm{Kn}^{\Delta}/_{\lambda}}{1 + 0.75\, \mathrm{Kn}^{-1} + \mathrm{Kn}^{\Delta}/_{\lambda}},$$

<div align="right">Eq. (A13)</div>

where λ is the mean free path defined here as $\lambda = \frac{3\, D_{gas}^X}{\bar{c}\, r}$. This shows that the "compartmentalized" or coupled-equilibria approach for describing near-gas concentrations within a shell of length Δ results in exactly the results of Fuchs & Sutugin[33] when integrating the steady-state condition for the concentration profile at position $r + \Delta$ with boundary conditions set by an equivalent flux matching condition.

Given that Eq. (A13) maps onto the description of Fuchs & Sutugin,[33] this description agrees with the "Fuchs correction" used to account for diffusional "resistance" in the widely-applied resistor formulation of multiphase kinetics.[27, 53, 54] We note, however, that the Fuchs correction follows the expanded method outlined by Fuchs & Sutugin[33] in which Eq. (A13) is slightly adapted to agree with numerical solutions to the Boltzmann equation across the Kn range. For completeness, we include this adapted transport term,

$$\frac{J}{J_k} = \frac{1 + \mathrm{Kn}^{\Delta}/_{\lambda}}{1 + 0.283 + 0.75\, \mathrm{Kn}^{-1} + \mathrm{Kn}^{\Delta}/_{\lambda}} = \gamma_{fuchs},$$

<div align="right">Eq. (A14)</div>

which includes an additional constant 0.283. We note that typically, the boundary sphere distance Δ is typically chosen to equal approximately the mean free path λ which further simplifies Eq. (A12). As shown in Fig. 6A, the transport terms found in Eq. (A7), Eq. (A12), and Eq. (A14) are all numerically close to each other, differing only modestly in the transition regime.

To summarize, our standard method for treating diffusion yields the following coefficients,

$$k_{diff}^{gas} = \frac{D_{gas}^X}{r\, \delta},$$

<div align="right">Eq. (A15)</div>

$$k_{col} = k_{ads} \frac{\Gamma_X^{\infty}}{\delta} = \frac{\bar{c}}{4\, \delta},$$

<div align="right">Eq. (A16)</div>

29

which, when analyzed in light of mechanistic steps AR1 and AR2, yields an identical gas-to-surface transport efficiency as described by the simplest case from Fuchs & Sutugin[33] with the boundary sphere distance $\Delta = 0$. To account for a nonzero boundary-sphere thickness Δ, the rate coefficient for the diffusional process above can be modified to include the flux at distance $r + \Delta$, respective to the surface region by dividing by the surface volume:

$$k_{diff}^{gas} = \frac{4\pi\, D_{gas}^X (r+\Delta)}{4\pi\, r^2\, \delta} = \frac{D_{gas}^X (r+\Delta)}{r^2\, \delta} \qquad\qquad \text{Eq. (A17)}$$

$$k_{col} = \frac{4\pi\, r^2\, \bar{c}/4}{4\pi\, r^2\, \delta} = \frac{\bar{c}}{4\,\delta}. \qquad\qquad \text{Eq. (A18)}$$

Fig. 6A summarizes these observations, providing results from Eqs. (A7) and (A12) compared to the Fuchs Correction Eq. (A14). For reference, Fig. 6B evaluates the radial dependence of k_{col} and k_{diff}^{gas} with $\bar{c} = 360$ m/s, $D_{gas}^X = 0.18$ cm^2/s, and $\delta = 1$ nm.

30
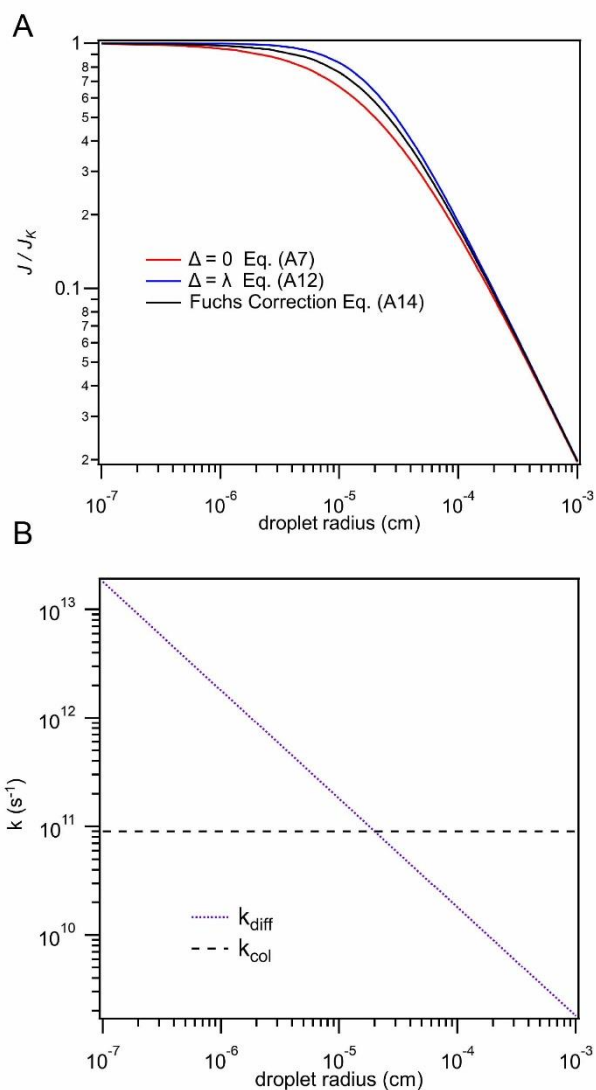
Figure 6: (A) Comparison of diffusional descriptions, showing the fraction of collisional-type flux vs. droplet radius for the three descriptions in Eqs. (A7), (A12), and (A14). (B) Radial dependence of the kinetic coefficients k_{diff} and k_{col}.

SYMBOLS AND NOTATION

g	Subscript denoting gas
gs	Subscript denoting gas-surface
sb	Subscript denoting surface-bulk
blk	Bulk Liquid
srf	Superscript denoting surface

31

ads	Subscript denoting adsorbed species at interface
rd	Subscript denoting reacto-diffusive dimension
core	Subscript denoting adsorbed species in core of the droplet
$\bar{c}$	Mean speed of X (cm/s)
X	Trace gas
Y	Solute in droplet
H_{cc}^{gb}	Dimensionless Henry's Law constant linking gas and bulk concentrations of X.
H_{cc}^{gs}	Dimensionless Henry's Law constant linking gas and interface concentrations of X.
H_{cc}^{sb}	Dimensionless Henry's Law constant linking surface and bulk concentrations of X.
K_{eq}^{Y}	Langmuir Equilibrium Constant for Y (cm^3 molec.$^{-1}$)
D^{X}	Diffusion constant of X (cm^2 s^{-1})
k_{ads}	Adsorption rate coefficient (cm^3 molec.$^{-1}$ s^{-1}) for X
k_{des}	Desorption rate coefficient (s^{-1}) for X
$k_{Xdesolv}$	Desolvation rate coefficient (cm^3 molec.$^{-1}$ s^{-1}) for X
$k_{Ydesolv}$	Desolvation rate coefficient (cm^3 molec.$^{-1}$ s^{-1}) for Y
k_{Xsolv}	Solvation rate coefficient (s^{-1}) for X
k_{Ysolv}	Solvation rate coefficient (s^{-1}) for Y
k_{rxn}	Reaction rate coefficient (cm^3 molec.$^{-1}$ s^{-1})
k_{Xdiff}	Diffusion rate constant of X (s^{-1})
$\Gamma_{\infty(X/Y)}$	Maximum surface concentration (molec. cm^{-2}) of X or Y
δ	Interface thickness (cm)
L_{rd}	Reacto-diffusive length (cm)
L_{rd}'	Transition function (cm)
γ	Uptake coefficient

r	Radius (cm)
V	Volume (cm^3)
$\boldsymbol{W}\{x\}$	Lambert W function

Supporting Information: Sec. SI-1 and Fig. S1 compares the transition function shown Eq (2) with L_{rd}. Sec. SI-2 shows the full derivation of the closed form expressions in Eqs. (21)-(23). Sec. SI-3 and Table S1 provides the experimental details, rate and diffusion coefficients for validation of the model with the experimental data shown in Figs. 4 and 5.

AUTHOR DECLARATIONS

Conflict of Interest

The authors have no conflicts to disclose

DATA AVAILABILITY

The data that support the findings of this study are available from the corresponding author upon reasonable request.

References:

1. F. Riccobono, S. Schobesberger, C. E. Scott, J. Dommen, I. K. Ortega, L. Rondo, J. Almeida, A. Amorim, F. Bianchi, M. Breitenlechner*, et al.*, Oxidation Products of Biogenic Emissions Contribute to Nucleation of Atmospheric Particles, *Science*, 2014, **344**, 717-721.

2. J. P. D. Abbatt and A. R. Ravishankara, Opinion: Atmospheric multiphase chemistry – past, present, and future, *Atmos. Chem. Phys.*, 2023, **23**, 9765-9785.

3. J.-M. Choi, A. S. Holehouse and R. V. Pappu, Physical Principles Underlying the Complex Biology of Intracellular Phase Transitions, *Ann. Rev. Biophys.*, 2020, **49**, 107-133.

4.   Y. Shin and C. P. Brangwynne, Liquid phase condensation in cell physiology and disease, *Science*, 2017, **357**, eaaf4382.

5.   A. Simon, G. Amy and M. Tanja, Considerations and Challenges in Studying Liquid-Liquid Phase Separation and Biomolecular Condensates, *Cell*, 2019, **176**, 419-434.

6.   S. M. Dischinger, D. J. Miller, D. A. Vermaas and R. S. Kingsbury, Unifying the Conversation: Membrane Separation Performance in Energy, Water, and Industrial Applications, *ACS ES&T Engineering*, 2024, **4**, 277-289.

7.   K. R. Wilson, A. M. Prophet, G. Rovelli, M. D. Willis, R. J. Rapf and M. I. Jacobs, A kinetic description of how interfaces accelerate reactions in micro-compartments, *Chem. Sci.*, 2020, **11**, 8533-8545.

8.   E. K. Brown, G. Rovelli and K. R. Wilson, pH jump kinetics in colliding microdroplets: accelerated synthesis of azamonardine from dopamine and resorcinol, *Chem. Sci.*, 2023, **14**, 6430-6442.

9.   A. M. Deal, A. M. Prophet, F. Bernal, R. J. Saykally and K. R. Wilson, A Detailed Reaction Mechanism for Thiosulfate Oxidation by Ozone in Aqueous Environments, *Environ. Sci. Technol.*, 2024, **58**, 18959-18968.

10.   A. M. Prophet, K. Polley, E. K. Brown, D. T. Limmer and K. R. Wilson, Distinguishing Surface and Bulk Reactivity: Concentration-Dependent Kinetics of Iodide Oxidation by Ozone in Microdroplets, *J. Phys. Chem. A*, 2024, **128**, 8970-8982.

11.   M. D. Willis and K. R. Wilson, Coupled Interfacial and Bulk Kinetics Govern the Timescales of Multiphase Ozonolysis Reactions, *J. Phys. Chem. A*, 2022, **126**, 4991-5010.

12.   K. R. Wilson, A. M. Prophet and M. D. Willis, A Kinetic Model for Predicting Trace Gas Uptake and Reaction, *J. Phys. Chem. A*, 2022, **126**, 7291-7308.

13.   W. Hinsberg, Houle, F., Kinetiscope - A Stochastic kinetics simulator, https://hinsberg.net/kinetiscope/authors.html, (accessed 01-21, 2025).

14.   C. Pfrang, M. Shiraiwa and U. Pöschl, Coupling aerosol surface and bulk chemistry with a kinetic double layer model (K2-SUB): oxidation of oleic acid by ozone, *Atmos. Chem. Phys.*, 2010, **10**, 4537-4557.

15.   M. Shiraiwa, R. M. Garland and U. Pöschl, Kinetic double-layer model of aerosol surface chemistry and gas-particle interactions (K2-SURF): Degradation of polycyclic aromatic hydrocarbons exposed to O_3, NO_2, H_2O, OH and NO_3, *Atmos. Chem. Phys.*, 2009, **9**, 9571-9586.

16.   M. Shiraiwa, C. Pfrang, T. Koop and U. Pöschl, Kinetic multi-layer model of gas-particle interactions in aerosols and clouds (KM-GAP): linking condensation, evaporation and chemical reactions of organics, oxidants and water, *Atmos. Chem. Phys.*, 2012, **12**, 2777-2794.

17. M. Shiraiwa, C. Pfrang and U. Pöschl, Kinetic multi-layer model of aerosol surface and bulk chemistry (KM-SUB): the influence of interfacial transport and bulk diffusion on the oxidation of oleic acid by ozone, *Atmos. Chem. Phys.*, 2010, **10**, 3673-3691.

18. S. Ingram, G. Rovelli, Y.-C. Song, D. Topping, C. S. Dutcher, S. Liu, L. Nandy, M. Shiraiwa and J. P. Reid, Accurate Prediction of Organic Aerosol Evaporation Using Kinetic Multilayer Modeling and the Stokes–Einstein Equation, *J. Phys. Chem. A*, 2021, **125**, 3444-3456.

19. P. Roldin, A. C. Eriksson, E. Z. Nordin, E. Hermansson, D. Mogensen, A. Rusanen, M. Boy, E. Swietlicki, B. Svenningsson, A. Zelenyuk and J. Pagels, Modelling non-equilibrium secondary organic aerosol formation and evaporation with the aerosol dynamics, gas- and particle-phase chemistry kinetic multilayer model ADCHAM, *Atmos. Chem. Phys.*, 2014, **14**, 7953-7993.

20. A. M. Prophet, K. Polley, G. J. Van Berkel, D. T. Limmer and K. R. Wilson, Iodide oxidation by ozone at the surface of aqueous microdroplets, *Chem. Sci.*, 2024, **15**, 736-756.

21. R. Vacha, P. Slavicek, M. Mucha, B. J. Finlayson-Pitts and P. Jungwirth, Adsorption of Atmospherically Relevant Gases at the Air/Water Interface: Free Energy Profiles of Aqueous Solvation of N2, O2, O3, OH, H2O, HO2, and H2O2, *J. Phys. Chem. A*, 2004, **108**, 11573-11579.

22. J. Vieceli, M. Roeselova, N. Potter, L. X. Dang, B. C. Garrett and D. J. Tobias, Molecular Dynamics Simulations of Atmospheric Oxidants at the Air-Water Interface: Solvation and Accommodation of OH and O3, *J. Phys. Chem. B*, 2005, **109**, 15876-15892.

23. P. V. Danckwerts, Absorption by simultaneous diffusion and chemical reaction into particles of various shapes and into falling drops, *Trans. Faraday Soc.*, 1951, **47**, 1014-1023.

24. P. V. Danckwerts, *Gas-liquid reactions*, John Wiley & Sons, Ltd, 1971.

25. S. E. Schwartz, *Mass-Transport Considerations Pertinent to Aqueous Phase Reactions of Gases in Liquid-Water Clouds*, NATO ASI Series: Chemistry of Multiphase Atmospheric Systems, Springer Berlin Heidelberg, Berlin, Heidelberg, 1986.

26. B. Shi and J. H. Seinfeld, On mass transport limitation to the rate of reaction of gases in liquid droplets, *Atmos. Environ. A, Gen. Top.*, 1991, **25**, 2371-2383.

27. D. R. Worsnop, J. W. Morris, Q. Shi, P. Davidovits and C. E. Kolb, A chemical kinetic model for reactive transformations of aerosol particles, *Geophys. Res. Lett.*, 2002, **29**, 57-51-57-54.

28. G. M. Nathanson, P. Davidovits, D. R. Worsnop and C. E. Kolb, Dynamics and kinetics at the gas-liquid interface, *J. Phys. Chem.*, 1996, **100**, 13007-13020.

29. J. H. Lambert, Observations variae in mathesin puram., *Acta. Helv.*, 1758, **3**, 128-168.

30. J. F. Pedrayes, M. G. Melero, J. M. Cano, J. G. Norniella, S. B. Duque, C. H. Rojas and G. A. Orcajo, Lambert W function based closed-form expressions of supercapacitor electrical variables in constant power applications, *Energy*, 2021, **218**, 119364.

31. J. H. Seinfeld and S. N. Pandis, *Atmospheric Chemistry and Physics: From Air Pollution to Climate Change*, Wiley, 2016.

32. J. Crank, *The Mathematics of Diffusion*, Clarendon Press, 1979.

33. N. A. Fuchs and A. G. Sutugin, in *Topics in Current Aerosol Research*, eds. G. M. Hidy and J. R. Brock, Pergamon, 1971, DOI: https://doi.org/10.1016/B978-0-08-016674-2.50006-6, p. 1.

34. I. Langmuir, The Adsorption of Gases on Plane Surfaces of Glass, Mica and Platinum, *J. Am. Chem. Soc.*, 1918, **40**, 1361-1403.

35. D. A. Knopf, M. Ammann, T. Berkemeier, U. Pöschl and M. Shiraiwa, Desorption lifetimes and activation energies influencing gas–surface interactions and multiphase chemical kinetics, *Atmos. Chem. Phys.*, 2024, **24**, 3445-3528.

36. D. R. Hanson, Surface-Specific Reactions on Liquids, *J. Phys. Chem. B*, 1997, **101**, 4998-5001.

37. R. G. Remorov and C. George, Analysis of chemical kinetics at the gas-aqueous interface for submicron aerosols, *Phys. Chem. Chem. Phys.*, 2006, **8**, 4897-4901.

38. K. Polley, K. R. Wilson and D. T. Limmer, On the Statistical Mechanics of Mass Accommodation at Liquid–Vapor Interfaces, *J. Phys. Chem. B*, 2024, **128**, 4148-4157.

39. G. Bleys and P. Joos, Adsorption kinetics of bolaform surfactants at the air/water interface, *J. Phys. Chem.*, 1985, **89**, 1027-1032.

40. P. B. Petersen and R. J. Saykally, Probing the Interfacial Structure of Aqueous Electrolytes with Femtosecond Second Harmonic Generation Spectroscopy, *J. Phys. Chem. B*, 2006, **110**, 14060-14073.

41. Y. Liu, Is the Free Energy Change of Adsorption Correctly Calculated?, *J. Chem. Eng. Data*, 2009, **54**, 1981-1985.

42. P. B. Petersen and R. J. Saykally, Adsorption of Ions to the Surface of Dilute Electrolyte Solutions: The Jones−Ray Effect Revisited, *J. Am. Chem. Soc.*, 2005, **127**, 15446-15452.

43. A. Fallah-Araghi, K. Meguellati, J.-C. Baret, A. E. Harrak, T. Mangeat, M. Karplus, S. Ladame, C. M. Marques and A. D. Griffiths, Enhanced Chemical Synthesis at Soft Interfaces: A Universal Reaction-Adsorption Mechanism in Microcompartments, *Phys. Rev. Lett.*, 2014, **112**, 028301.

44. P. Kim, R. S. Reynolds, A. M. Deal, V. Vaida, M. Ahmed and K. R. Wilson, Accelerated Zymonic Acid Formation from Pyruvic Acid at the Interface of Aqueous Nanodroplets, *J. Phys. Chem. Lett.*, 2024, **15**, 11131-11138.

45. M. Li, C. Boothby, R. E. Continetti and V. H. Grassian, Size-Dependent Sigmoidal Reaction Kinetics for Pyruvic Acid Condensation at the Air–Water Interface in Aqueous Microdroplets, *J. Am. Chem. Soc.*, 2023, **145**, 22317-22321.

46. M. Li, S. Yang, M. Rathi, S. Kumar, C. S. Dutcher and V. H. Grassian, Enhanced condensation kinetics in aqueous microdroplets driven by coupled surface reactions and gas-phase partitioning, *Chem. Sci.*, 2024, **15**, 13429-13441.

47. B. J. Dennis-Smither, F. H. Marshall, R. E. Miles, T. C. Preston and J. P. Reid, Volatility and oxidative aging of aqueous maleic acid aerosol droplets and the dependence on relative humidity, *J. Phys. Chem. A*, 2014, **118**, 5680-5691.

48. O. R. Hunt, A. D. Ward and M. D. King, Heterogeneous oxidation of nitrite anion by gas-phase ozone in an aqueous droplet levitated by laser tweezers (optical trap): is there any evidence for enhanced surface reaction?, *Phys. Chem. Chem. Phys.*, 2015, **17**, 2734-2741.

49. *Wolfram Research, Inc., Mathematica*, Champaign, Illinois, Version 13.0.0 edn., 2021.

50. A. Prophet, D. Limmer and K. Wilson, Surfactant Control of Interfacial Reaction Rates in Aqueous Microdroplets, *ChemRxiv*, 2024, DOI: 10.26434/chemrxiv-2024-mj9gg.

51. C. E. Kolb, R. A. Cox, J. P. D. Abbatt, M. Ammann, E. J. Davis, D. J. Donaldson, B. C. Garrett, C. George, P. T. Griffiths, D. R. Hanson, *et al.*, An overview of current issues in the uptake of atmospheric trace gases by aerosols and clouds, *Atmos. Chem. Phys.*, 2010, **10**, 10561-10605.

52. I. B. A. Smokers, B. S. Visser, A. D. Slootbeek, W. T. S. Huck and E. Spruijt, How Droplets Can Accelerate Reactions─Coacervate Protocells as Catalytic Microcompartments, *Acc. Chem. Res.*, 2024, **57**, 1885-1895.

53. D. R. Hanson, A. R. Ravishankara and E. R. Lovejoy, Reaction of BrONO2 with H2O on submicron sulfuric acid aerosol and the implications for the lower stratosphere, *J. Geophys. Res.: Atmos*, 1996, **101**, 9063-9069.

54. C. E. Kolb, P. Davidovits, J. T. Jayne, Q. Shi and D. R. Worsnop, Kinetics of Trace Gas Uptake by Liquid Surfaces, *Progress in Reaction Kinetics and Mechanism*, 2002, **27**, 1-46.